iScience

CellPress
OPEN ACCESS

Article

Phosphoglycerate Mutase Cooperates with Chk1 Kinase to Regulate Glycolysis

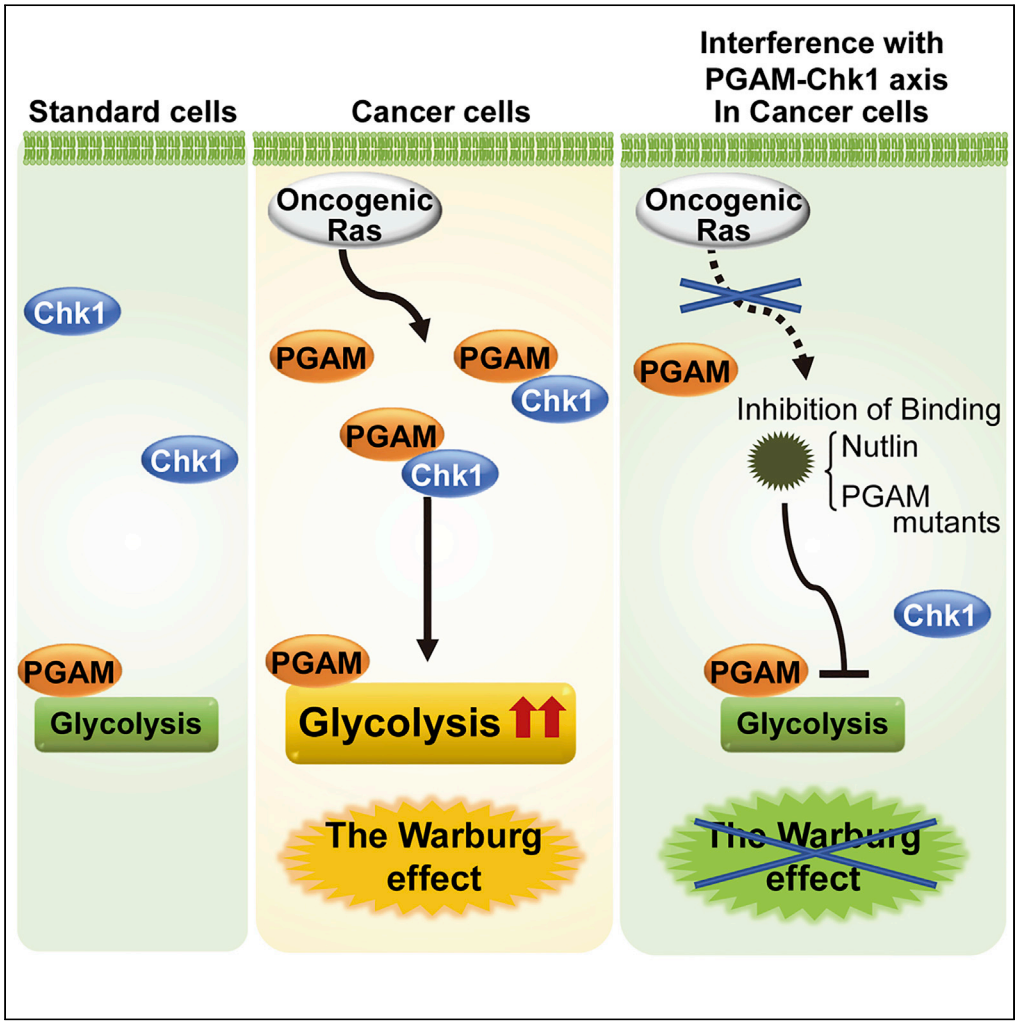

Takumi Mikawa, Eri Shibata, Midori Shimada, ..., Nobuya Inagaki, Masayuki Yokode, Hiroshi Kondoh

hkondoh@kuhp.kyoto-u.ac.jp

HIGHLIGHTS

PGAM cooperates with Chk1 kinase to boost glycolysis in a non-enzymatic manner

PGAM interacts with Chk1 in cancer with oncogenic Ras but not in standard cells

Chemical and genetical interference with PGAM-Chk1 axis abrogates the Warburg effect

Mikawa et al., iScience 23, 101306
July 24, 2020
https://doi.org/10.1016/j.isci.2020.101306

iScience

CellPress
OPEN ACCESS

Article

Phosphoglycerate Mutase Cooperates with Chk1 Kinase to Regulate Glycolysis

Takumi Mikawa,[1,2] Eri Shibata,[1,2] Midori Shimada,[3] Ken Ito,[1,2] Tomiko Ito,[1,2] Hiroaki Kanda,[4] Keiyo Takubo,[5] Matilde E. Lleonart,[6] Nobuya Inagaki,[2] Masayuki Yokode,[1,7] and Hiroshi Kondoh[1,2,8,*]

SUMMARY

Dysregulated glycolysis, including the cancerous Warburg effect, is closely involved in pathological mechanisms of diseased states. Among glycolytic enzymes, phosphoglycerate mutase (PGAM) has been known to exert certain physiological impact *in vitro*, whereas its regulatory role on glycolysis remains unclear. Here, we identified that PGAM plays a key role in regulating glycolysis in cancer cells but not in standard cells. Cancer-prone phenotype by PGAM overexpression *in vivo* was associated with upregulated glycolytic features. PGAM interacts and cooperates with Chk1 to regulate the enhanced glycolysis in cancer cells, especially under oncogenic Ras expressing conditions. Genetic or chemical interference of the PGAM-Chk1 interaction, with intact PGAM activity, abrogated the maintenance of cancerous enhanced glycolysis. Thus, the nonenzymatic function of PGAM is essential for the Warburg effect that accompanies cancerous proliferation.

INTRODUCTION

Glycolysis constitutes an essential metabolism among various organisms, serving not only as an energy source but also for the synthesis of macromolecules (Vander Heiden et al., 2009). The regulation of glycolysis depends on several factors including growth conditions, differentiation status, and environmental stress. In mammalian cells, metabolic adaptation in glycolysis is mediated partly by the activation of specific signaling modules, followed by the transcriptional upregulation of glycolytic enzymes (Dang and Semenza, 1999). In addition to transcriptional factors, several other molecules including signals from nutritional stress, oncogenic stimuli, and posttranscriptional regulators are also deeply involved in glycolytic regulation (Mikawa et al., 2015).

Fine-tuning of glycolysis is required to maintain physiological homeostasis in normal cells and tissues, and dysregulated glycolysis is closely related to pathological features. Impaired glycolysis *in vivo* is associated with dysfunction in various tissues and degenerative disorders (Goyal et al., 2017; Taylor et al., 2001). Conversely, the pathological enhancement of glycolysis is also observed in several diseased states, such as inflammation (Chimenti et al., 2015), ischemia, and the cancerous Warburg effect in association with increase of activity and protein levels for multiple glycolytic enzymes (Warburg, 1956). Although normal cells may adapt to hypoxic conditions by enhancing anaerobic glycolysis and limiting energy demands, cancer cells *in vivo* continue to grow even in hypoxia, which requires excess glycolysis as a maladaptive metabolism in the core of solid tumors. However, the Warburg effect cannot be explained simply as a consequence of cellular adaptation to hypoxia, as cancer cells maintain enhanced glycolysis even in standard tissue culture conditions (20% oxygen) or in circulating blood (Koppenol et al., 2011). Therefore, a rising question is how the Warburg effect is linked to the other cancerous properties besides adaptation to hypoxia.

Phosphoglycerate mutase (PGAM) is a glycolytic enzyme that converts 3-phosphoglycerate into 2-phosphoglycerate as an isomerase (Rodwell et al., 1957). PGAM consists of two isoforms, PGAM1 and PGAM2, termed also as brain- and muscle-forms, respectively, both of which display a significant similarity in their sequences (79% identity) and enzymatic activities (Kondoh et al., 2005; Mikawa et al., 2014; Zhang et al., 2001). Recent reports suggest that PGAM represents a key factor connecting glycolysis to physiological homeostasis. PGAM supports anti-oxidative defense not only by the reduction of mitochondrial reactive oxygen species (Kondoh et al., 2005, 2007) but also via activation of the pentose phosphate pathway

[1]Geriatric Unit, Graduate School of Medicine, Kyoto University, 54 Kawaharacho, Shogoin, Sakyo-ku, Kyoto 606-8507, Japan

[2]Department of Diabetes, Endocrinology and Nutrition, Graduate School of Medicine, Kyoto University, Kyoto 606-8507, Japan

[3]Joint Faculty of Veterinary Science, Yamaguchi University, Yamaguchi 753-8511, Japan

[4]Department of Pathology, Saitama Cancer Center, Saitama 362-0806, Japan

[5]Department of Stem Cell Biology, Research Institute, National Center for Global Health and Medicine, Tokyo 162-8655, Japan

[6]Department of Pathology, Hospital Vall de'Hebron, Barcelona 08035, Spain

[7]Department of Clinical Innovative Medicine, Translational Research Center, Graduate School of Medicine, Kyoto University, Kyoto 606-8507, Japan

[8]Lead Contact

*Correspondence: hkondoh@kuhp.kyoto-u.ac.jp

https://doi.org/10.1016/j.isci.2020.101306

(Hitosugi et al., 2012). Moreover, the p53/Mdm2 axis promotes proteolysis of PGAM during senescence-inducing stress (Mikawa et al., 2014), which is consistent with reports that p53 inactivation enhances glycolysis in cancer (Bensaad and Vousden, 2007). In addition to the ubiquitination, PGAM activity is post transcriptionally modulated by the phosphorylation or acetylation (Wang et al., 2017; Xu et al., 2014). Several studies also implicate the involvement of PGAM in human disease. Although PGAM protein and activity are upregulated in many cancerous tissues (Durany et al., 1997), patients with PGAM deficiencies are also reported (Naini et al., 2009). However, the precise regulatory role of PGAM in glycolysis remains unclear.

Here, we report a previously unappreciated role for PGAM in cancerous glycolytic regulation. We observed that PGAM significantly affected the global profiles of glycolysis in cancerous cells. PGAM cooperated with Chk1, previously known as a checkpoint kinase for p53, to boost glycolysis under oncogenic conditions, but not in standard cells. The significance of the PGAM-Chk1 interaction in cancerous glycolysis was validated by several lines of evidence with genetic or chemical ablation of PGAM-Chk1 binding, especially under oncogenic Ras expressing conditions. Thus, PGAM and Chk1 cooperated to regulate cancerous glycolysis.

RESULTS

PGAM Overexpression *In Vivo* Promotes Chemically Induced Tumorigenesis with Global Increase in Glycolytic mRNAs

We previously reported that heart-specific *Pgam2*-transgenic (Tg) mice displayed almost normal glycolytic features in the heart (Okuda et al., 2013). However, the impact of global PGAM overexpression *in vivo* remains unclear. As it has been demonstrated that the overexpression of either PGAM isoform confers similar physiological impact (Kondoh et al., 2005; Mikawa et al., 2014; Zhang et al., 2001), we utilized *Pgam2*-Tg mice, which exhibited a significant increase of PGAM protein in the whole body by the *CAG*-promoter driven *Pgam2-FLAG* transgene (Figure S1A) (Mikawa et al., 2014). Global overexpression of PGAM *in vivo* did not affect the profiles for glycolytic mRNAs among the various tissues (skin, liver, kidney, muscle, WAT, lung, or heart) under physiological conditions or in MEFs under standard culture conditions (Figures S1B and S1C). Although both isoforms of PGAM were expressed in skin of wild-type mice (Mikawa et al., 2014), however, we noticed that skin in *Pgam2*-Tg mice was more vulnerable to inflammation caused by a proinflammatory agent, 12-O-tetradecanoylphorbol-13-acetate (TPA) (Figures S2A and S2B). These findings prompted further investigation into the possibility that PGAM overexpression *in vivo* may affect glycolysis under TPA stress. For this purpose, we applied a protocol of chemically induced carcinogenesis utilizing 7,12-dimethylbenz[a]anthracene (DMBA) initiation followed by TPA promotion in mice skin from control and *Pgam2*-Tg mice (Figure S2C). We observed that the total number of tumors in *Pgam2*-Tg mice was slightly increased (Figure S2D), whereas the tumor sizes were strikingly larger than those of control mice throughout the protocol. At the early stage of the experimental process (8–12 weeks) small tumors in *Pgam2*-Tg mice were already observed (Figure 1A, top panel). Subsequently (12–24 weeks), some tumors in the *Pgam2*-Tg mice grew to over 6 mm in their diameters, which was not observed in control mice (Figure 1A, middle and bottom panels). Notably, some of the largest tumors in the *Pgam2*-Tg mice were accompanied by moderate-to-severe ulceration as shown in Figure 1B. At the end of the protocol (24 weeks), pathologic analysis was performed for all tumors in mice. Histologically, tumors in both groups showed acanthosis and hyperkeratosis. All tumors in the control mice were pathologically benign (squamous cell papillomas), whereas 3 of 25 tumors that developed in *Pgam2*-Tg mice showed marked dyskeratosis, numerous mitoses, and severe disturbances of stratification, which are characteristic of squamous cell carcinoma (SCC) (Figures 1C and 1D).

Notably, we identified clear differences in the mRNA profiles of glycolytic enzymes in the skins of this setting. The levels of glycolytic mRNAs were markedly increased both in papillomas and in skins without tumors from *Pgam2*-Tg mice compared with those in control mice (Figure 1E). In addition, the expression of these mRNAs was further enhanced in malignant tumors from *Pgam2-Tg* skin than in benign papillomas of the same genetic background (Figure 1E). Thus, the overexpression of PGAM promotes the expression of glycolytic mRNAs *in vivo* in chemically induced tumorigenesis.

Abrogation of PGAM Decreases Glycolytic mRNAs in Cancer Cells but Not in Standard Cells *In Vitro*

We next examined the impact of PGAM inactivation on glycolytic profiles *in vitro*. First, *PGAM1* siRNA was transfected into cancer cell types in which *PGAM1* is dominantly expressed: non-small cell lung carcinoma (H1299) and squamous cell carcinoma of human skin (HSC-1) cell lines (Figures S3A–S3C). We observed that

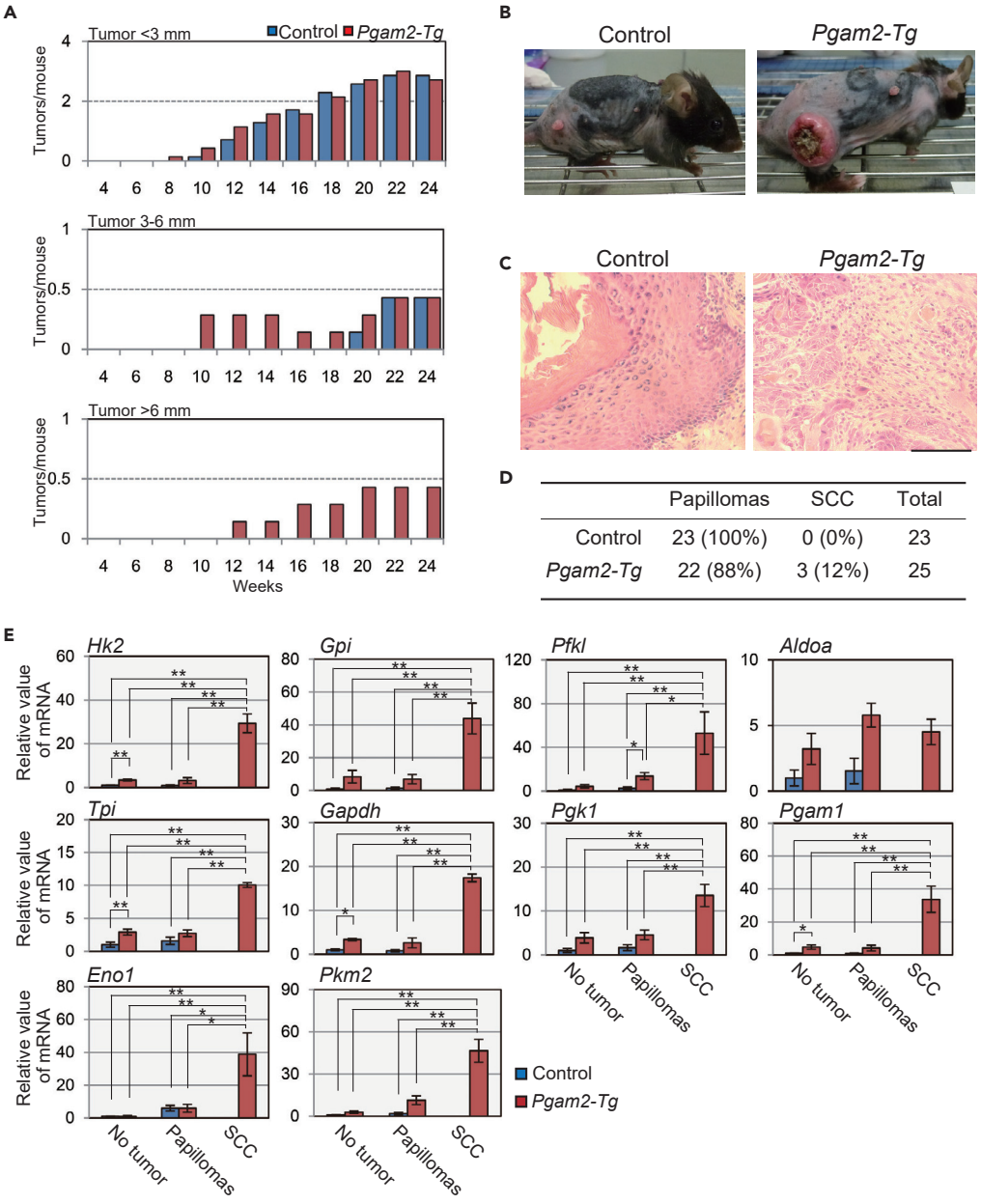

Figure 1. PGAM Overexpression *In Vivo* Promotes Chemically Induced Tumorigenesis with Significant Increment in Glycolytic mRNAs

Chemical-induced skin tumorigenesis was performed. Control (n = 7) and *Pgam2-Tg* mice (n = 7) were first treated with DMBA followed by TPA treatment twice a week.

(A) Comparison of tumor numbers between control (wild-type) and *Pgam2-Tg* mice. Tumors were classified into three subgroups according to their diameters (top panel for tumor size <3 mm; middle panel, 3–6 mm; and bottom panel, >6 mm). The average number of tumors per mouse was compared at the indicated time points.

(B) Representative tumors in control or *Pgam2-Tg* mice at 24 weeks are indicated.

(C and D) Histopathological analysis of skin tumors. (C) Skin papillomas in control (left panel) and SCC in *Pgam2-Tg* (right panel) with hematoxylin and eosin staining. Scale bar indicates 200 μm. (D) Summary of pathologic diagnoses of skin tumors in control and *Pgam2-Tg* mice.

(E) Comparison of mRNA levels for glycolytic enzymes between control and *Pgam2-Tg* mice. The results in non-tumor forming skin, skin papillomas, and skin SCCs are shown. Data for the indicated genes are shown as relative values against the counterparts in non-tumor-forming skin from control mice. Abbreviations for glycolytic enzymes were shown in Figure S1. *$p < 0.05$ and **$p < 0.005$, Dunnett's multiple comparison test. Data represent the mean ± SEM.

See also Figures S1 and S2.

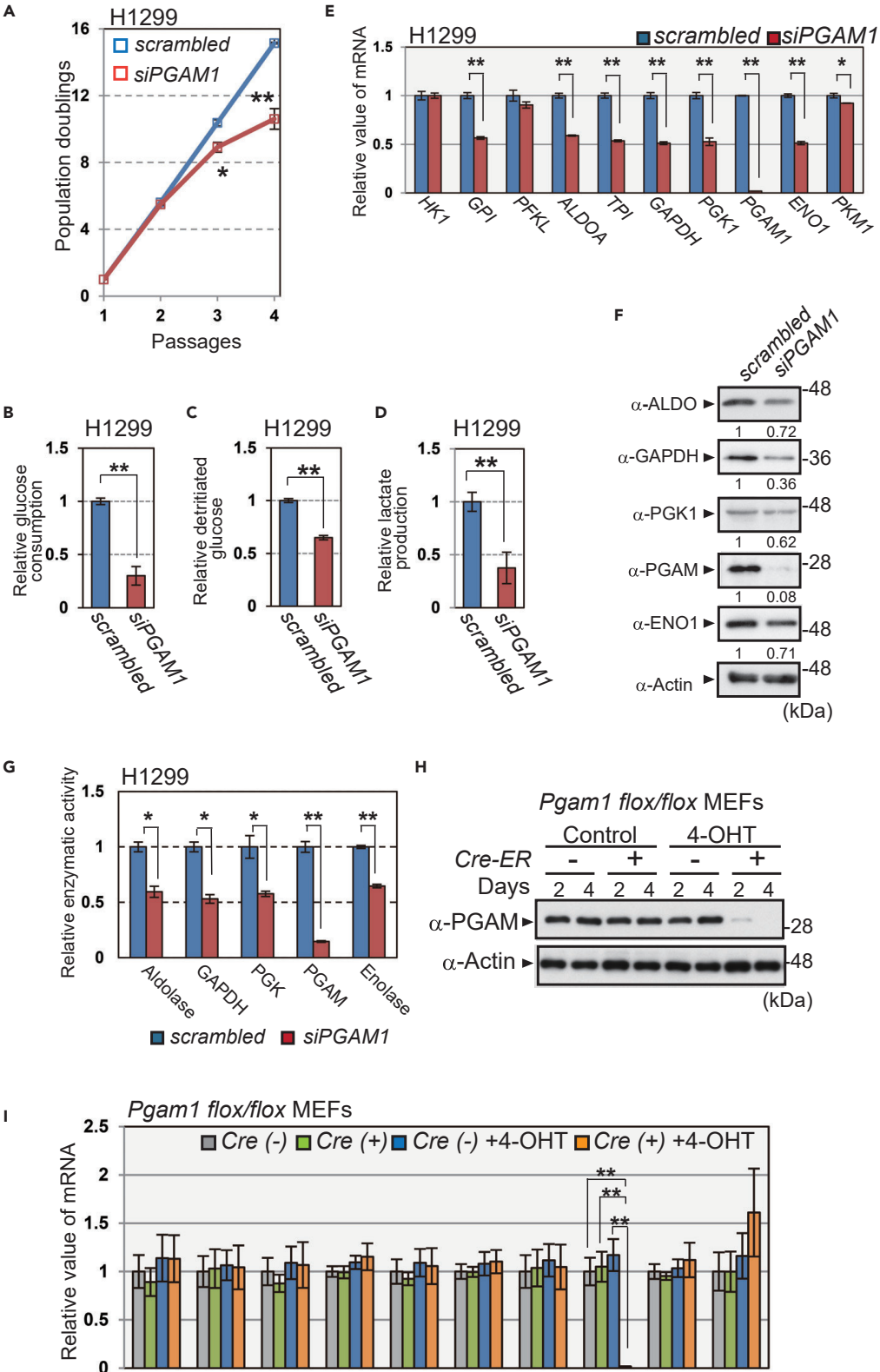
A
H1299
scrambled
siPGAM1
Population doublings
Passages
E
H1299
scrambled siPGAM1
Relative value of mRNA
HK1 GPI PFKL ALDOA TPI GAPDH PGK1 PGAM1 ENO1 PKM1
B
H1299
Relative glucose consumption
C
H1299
Relative detritiated glucose
D
H1299
Relative lactate production
F
scrambled siPGAM1
α-ALDO
α-GAPDH
α-PGK1
α-PGAM
α-ENO1
α-Actin
(kDa)
G
H1299
Relative enzymatic activity
Aldolase GAPDH PGK PGAM Enolase
scrambled siPGAM1
H
Pgam1 flox/flox MEFs
Control 4-OHT
Cre-ER
Days
α-PGAM
α-Actin
(kDa)
I
Pgam1 flox/flox MEFs
Cre (-) Cre (+) Cre (-) +4-OHT Cre (+) +4-OHT
Relative value of mRNA
Hk1 Gpi Pfkl Aldoa Tpi Gapdh Pgk1 Pgam1 Eno1 Pkm1

Figure 2. Ablation of PGAM Downregulates Glycolysis *In Vitro*

The impact of *PGAM1* knockdown on glycolysis in cancer cells *in vitro*. H1299 cells were transfected with *siPGAM1* (n = 3) or *scrambled* RNA (n = 3) (A–G).

(A) *PGAM1*-knockdown H1299 cells were passaged according to 3T3 cell culture protocol. The proliferation curves show population doublings. The glycolytic profiles were evaluated in *PGAM1*-knockdown H1299 cells (B–G).

(B–D) Glucose consumption was evaluated by measuring glucose concentration in medium (B), whereas glycolytic flux was evaluated using ^{3}H-labeled glucose (C). Lactate production was determined by the measurements of lactate concentration in medium (D).

(E) The mRNA levels for glycolytic enzymes were assessed. Data are relative to those in *scrambled* RNA-transfected H1299 cells. *p < 0.05 and **p < 0.005, Student's t test.

(F) The protein levels of the indicated glycolytic enzymes were analyzed by immunoblot using anti-aldolase (ALDO), anti-GAPDH, anti-PGK1, anti-PGAM, anti-enolase1 (ENO1), and anti-actin antibodies. Intensity of immunoblotting bands was normalized to that of actin. Relative values were shown, compared with *scrambled* RNA-transfected H1299 cells.

(G) Enzymatic activity of aldolase, GAPDH, PGK, PGAM, and enolase was measured by spectrometric assay.

(H and I) *Pgam1* was ablated in primary MEFs from *Pgam1*$^{flox/flox}$ mice harboring *Cre-ER* by treatment with 4-hydroxytamoxifen (4-OHT) for 4 days. (H) PGAM protein levels in the indicated MEFs were analyzed by immunoblotting. (I) Comparison of glycolytic mRNAs among the indicated MEFs after 4-OHT treatment (n = 3). *Cre(−)*; *Pgam1*$^{flox/flox}$ MEFs, *Cre(+)*; *Pgam1*$^{flox/flox}$ + *Cre-ER* MEFs.

Data are relative to those in control. *p < 0.05 and **p < 0.005, Dunnett's multiple comparison test. Data represent the mean ± SEM.

See also Figures S3 and S4.

PGAM1 knockdown in these cells significantly decreased their proliferative capacities (Figures 2A and S3D), accompanied by a marked reduction in glycolytic measurements such as glucose consumption, glycolytic flux, and lactate production (Figures 2B–2D and S3E–S3G). We observed that mRNA, protein levels, and enzymatic activities of other glycolytic enzymes were also reduced in both cell lines (Figures 2E–2G and S3H–S3J). Notably, the decline in overall glycolytic mRNAs after *PGAM1* knockdown was restored by ectopic expression of either mouse *Pgam1* or *Pgam2* (Figures S4A and S4B), probably due to the high similarity in their sequences and enzymatic activities.

Next, *Pgam1*$^{flox/flox}$ MEFs expressing *Cre*-ER were generated by crossing *CAG-Cre-ER*-Tg mice and *Pgam1*$^{flox/flox}$ mice, which we established (Figure S4C). *Pgam1* mRNA and protein were efficiently ablated after 4-hydroxytamoxifen (4-OHT) treatment of these MEFs (Figures 2H and 2I), followed by a premature senescent growth arrest (Figures S4D and S4E). However, glycolytic mRNA expression in these cells was similar to *Pgam1*-intact cells (Figure 2I). Similar results were obtained following transfection with *Pgam1* siRNA in primary MEFs and human fibroblast WI-38 cells, which predominantly express PGAM1 (Figures S4F and S4G). Collectively, the abrogation of PGAM in standard cells did not affect the levels of other glycolytic mRNAs, in sharp contrast to our findings in cancer cells.

PGAM Attenuates p53 Phosphorylation and Interacts with Chk1

In addition to the susceptibility of globally PGAM-overexpressing mice to skin carcinogenesis (Figure 1), we previously reported that PGAM was ubiquitinated via the Mdm2/p53 axis under senescence-inducing stress (Mikawa et al., 2014). We also noticed that, in prematurely senescent MEFs by *Pgam1* ablation, the levels of several p53 targets (*p21*^{Cip}, *Bax*, and *Fas*) and *p16*^{ink4} were significantly increased (Figure 3A). To gain insights into the molecular mechanism of glycolytic regulation by PGAM, we further investigated the possible link between PGAM and the tumor suppressor p53. As p53 activity and protein stability are regulated largely by post-transcriptional modification including its phosphorylation, we examined the p53 profile under oncogenic stress both in *Pgam2*-Tg and control MEFs expressing Ras-G12V. The protein levels of p21 and Mdm2, downstream effectors of p53, were upregulated in Ras-G12V-expressing control MEFs but were moderately impaired in Ras-G12V-expressing *Pgam2*-Tg MEFs (Figure 3B). Oncogene-induced stress also upregulated p53 protein levels in control MEFs, accompanied by the enhanced phosphorylation of serine residues 18 and 23 (Di Micco et al., 2006). In contrast, in Ras-G12V-expressing *Pgam2*-Tg MEFs, p53 serine 23 phosphorylation was largely impaired compared with control, whereas serine 18 phosphorylation was moderately downregulated (Figure 3B). We also observed that ectopic expression of PGAM1 also suppresses p53 serine 23 phosphorylation in MEFs under oncogene-induced stress (Figure S5A). We also examined the DNA damage response in H1299 cell line with transfected WT p53. Similarly, p53 phosphorylation at serine 20, corresponding to serine 23 in mouse p53, was attenuated by ectopic PGAM expression during etoposide-induced DNA damage in H1299 cells (Figure S5B). These data indicate that PGAM partially interferes with p53 function by impacting phosphorylation at serine 23.

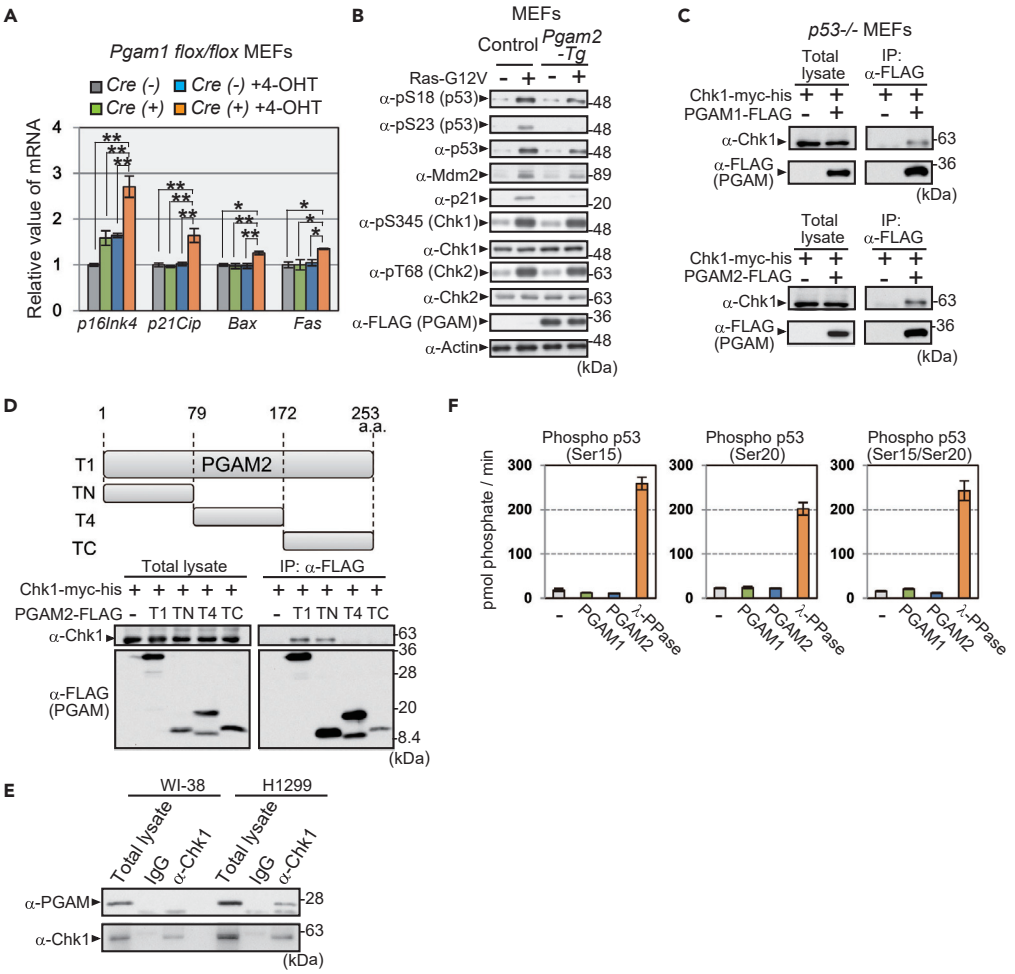

Figure 3. PGAM Interacts with and Modulates p53 Phosphorylation by Chk1

(A) The mRNA levels for *p16*^{Ink4} and p53 targets (*p21*^{Cip}, *Bax*, and *Fas*) were analyzed by quantitative PCR in the indicated MEFs. Indicated MEFs were treated with or without 4-OHT for 4 days, as in Figure 2H.

(B) The assessment for the effect of PGAM overexpression on the profiles of p53, Mdm2, p21, Chk1, and Chk2. Oncogenic Ras (Ras-G12V) was ectopically expressed in control (wild-type) and *Pgam2-Tg* MEFs via retroviral infection.

(C) Immunoprecipitation assay was performed using *p53*$^{-/-}$ MEFs expressing Chk1-myc-his with or without PGAM-FLAG. MEFs expressing PGAM1-FLAG (upper) or PGAM2-FLAG (lower) were examined. After treatment with 20 μM MG132 for 3 h, cells were lysed and immunoprecipitated with an anti-FLAG antibody and immunoblotted for Chk1 and FLAG.

(D) Schematic diagram of various fragments of PGAM2: full-length (T1), N-terminal (TN), middle-region (T4), and C-terminal (TC) fragments (upper panel). The binding of each fragment to Chk1 was assessed by co-immunoprecipitation (lower panels). Extracts from *p53*$^{-/-}$ MEFs transfected with the indicated plasmids were immunoprecipitated with an anti-FLAG antibody.

(E) Interaction between endogenous Chk1 and PGAM protein was evaluated with immunoprecipitation in H1299 and WI-38 cells.

(F) *In vitro* phosphatase activity against various peptides, phospho-p53 (Ser15), phospho-p53 (Ser20), and phospho-p53 (Ser15/Ser20) was determined using recombinant PGAM1, PGAM2, or λPPase. The peptide sequences of phospho-p53 are shown in Figure S5F. The amount of released phosphate from phosphopeptides was monitored.

*p < 0.05 and **p < 0.005, Dunnett's multiple comparison test. Data represent the mean ± SEM.

See also Figure S5.

p53 phosphorylation at serine 23 after DNA damage and oncogenic stress is mediated either by Chk1 or Chk2, checkpoint serine/threonine kinases, followed by p53 stabilization and activation (Shieh et al., 2000). In cells ectopically expressing PGAM, total protein levels and phosphorylation status of Chk1 and Chk2 (serine 345 and threonine 68, respectively) (Ahn et al., 2000; Zhao and Piwnica-Worms, 2001) were comparable with control cells (Figure 3B). However, we observed that both PGAM1 and PGAM2 physically

interacted with Chk1, but not with Chk2, in $p53^{-/-}$ MEFs, as shown with an immunoprecipitation assay (Figures 3C and S5C). To identify the Chk1-interacting domain in PGAM, a series of deletions in PGAM1- and PGAM2-FLAG were assessed for their ability to bind Chk1 (Figures S5D and 3D). Chk1-myc-his efficiently co-immunoprecipitated with full-length PGAM1- and 2-FLAG (T1) and the N-terminal one-third of PGAM (TN) but not with the other central (T4) or C-terminal fragments (TC). Consistently, endogenous PGAM protein co-immunoprecipitated with endogenous Chk1 protein in H1299 cancer cells but not in human standard cells WI-38 (Figure 3E).

Although PGAM has been shown to function as a phosphatase for metabolite (White and Fothergill-Gilmore, 1992), it is unclear whether PGAM possesses activity as a protein phosphatase. We assessed the potential of PGAM to display protein phosphatase activity. Recombinant PGAM1 or PGAM2 proteins with intact PGAM activity were prepared from *Escherichia coli* (Figure S5E). None of the recombinant PGAM proteins displayed any phosphatase activity against phospho-Ser/Thr peptides as a substrate, at any concentrations (125, 250, or 500 ng) or in any pH conditions tested (pH 6.2, 7.2, 8.2, and 9.2), whereas λPPase exhibited clear phosphatase activity (Figures S5F–S5H). In addition, recombinant PGAM proteins exhibited no phosphatase activity *in vitro* against phosphopeptides that mimicked phospho-p53 (Ser15, Ser20, or Ser15/Ser20; Figures 3F and S5F). Taken together, these data imply that PGAM interacts with and impairs p53 phosphorylation by Chk1, although PGAM is less likely to function as a protein phosphatase.

PGAM and Chk1 Cooperate to Regulate Glycolytic mRNAs

We noticed that the interaction of PGAM with Chk1 in $p53^{-/-}$ MEFs was enhanced under TPA stress (Figures 4A and S6A), which upregulates glycolytic mRNAs during *in vivo* chemical tumorigenesis protocol (Figure 1E). To investigate the physiological significance of the interaction between PGAM and Chk1, we evaluated the impact of Chk1 on glycolytic mRNA profiles *in vitro*. We observed that *Chk1* knockdown in the *p53*-null cell line H1299 was followed by a significant reduction in glucose consumption, glycolytic flux, and lactate production (Figures 4B–4D). Significant reductions in glycolytic mRNAs and proteins were also observed in these cells (Figures 4E and 4F). Treatment with the Chk1 kinase inhibitor UCN01, but not that with the Chk2 kinase inhibitor (Chk2-inhibitor II), induced the downregulation of glycolytic flux and glycolytic mRNAs in H1299 cells (Figures S6B and S6C). Interestingly, although a low concentration of UCN01 (50 nM) did not affect glycolytic mRNA levels in wild-type MEFs, the downregulation of glycolytic mRNAs was observed in $Pgam1^{+/-}$ MEFs (Figure 4G), which displayed the same glycolytic profiles and proliferative capacity as those in wild-type MEFs under standard culture condition (Figures S6D–S6G). These data support the notion that PGAM and Chk1 cooperatively affect glycolytic mRNA profiles.

Oncogenic Ras Pathway Is Required for the PGAM-Chk1 Interaction

To evaluate the clinical relevance of PGAM-Chk1 cooperation, the impact of PGAM/Chk1 axis on prognosis of patients with cancer was evaluated. According to the database of non-small cell lung cancer (NSCLC; jacob-00182-MSK) (Director's Challenge Consortium for the Molecular Classification of Lung Adenocarcinoma, et al., 2008) in PrognoScan (http://dna00.bio.kyutech.ac.jp/PrognoScan/) (Mizuno et al., 2009), we divided 104 patients with NSCLC into four groups in terms of the abundance of *PGAM1* and *Chk1* in cancers; Low-*PGAM1* + Low-*Chk1* (n = 23), Low-*PGAM1* + High-*Chk1* (n = 12), High-*PGAM1* + Low-*Chk1* (n = 29), and High-*PGAM1* + High-*Chk1* (n = 40) (Figure S7A). We noticed that the prognostic values were most significantly declined in High-*PGAM1* + High-*Chk1* group, compared with the others (Figure 5A).

Then, we addressed the question of whether the PGAM/Chk1 axis is involved in any cancer-related genetic events. In addition to H1299 and HSC-1 (Figures 2E and S3H), we evaluated the impact of *PGAM1* siRNA among thirteen other cancer cells, including skin, breast, colon, bone, and liver cancer cell lines. Among these 15 in total, four cancer cell lines (H1299, HSC-1, SW480, and DLD-1) displayed the most prominent changes in glycolytic mRNAs (*ALDO1*, *TPI*, *GAPDH*, and *ENO1*) following *PGAM1* knockdown (Figures 5B and S7B). For the clinical practice of precision medicine, subsets of oncogene and tumor suppressors are tested to select tailor-made therapy for individuals; for example, 50 cancer-related genes are listed according to Tsongalis et al. (2014) (Table S1). We surveyed 15 cancer cell lines we tested, regarding the mutations in these 50 cancer-related genes according to previous studies (Cancer Genome Atlas Research, 2008; Fujii et al., 1995; Hori et al., 2009; Klijn et al., 2015; Oliner et al., 1992). We noticed that aberrations both in the p53 and Ras pathways were the most common genetic features, shared in these four cell lines (H1299, HSC-1, SW480, and DLD-1) displaying significant glycolytic decline by *PGAM1* knockdown (Table S1). As patients with NSCLC with High-*PGAM1* + High-*Chk1* were classified in low-prognosis subgroup

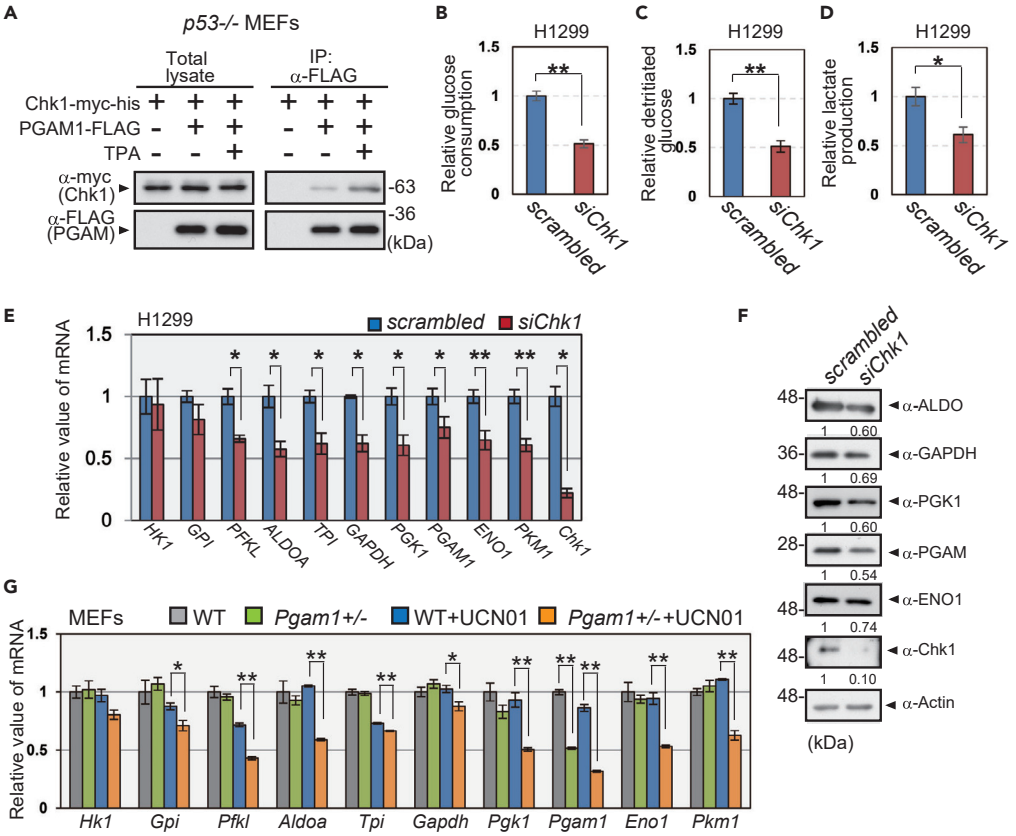

Figure 4. Cooperation between PGAM and Chk1 Regulates Glycolytic mRNAs

(A) The impact of TPA treatment on the interaction between PGAM1 and Chk1. $p53^{-/-}$ MEFs with expression of Chk1-myc-his and PGAM1-FLAG were treated with or without 0.1 μg/mL TPA for 48 h, followed by treatment with MG132 for 3 h. The cell lysates were immunoprecipitated with an anti-FLAG antibody.

(B–F) Impact of Chk1 inactivation on glycolytic profile *in Chk1* siRNA-transfected H1299 cells ($n = 3$). Glucose consumption, glycolytic flux, and lactate production were shown (B–D). The mRNA and protein levels of glycolytic enzymes were evaluated in indicated cells (E and F). Intensity of immunoblotting bands was normalized to that of actin. Relative values were shown, compared with *scrambled* RNA-transfected H1299 cells.

(G) Comparison of glycolytic mRNAs between WT ($n = 3$) and $Pgam1^{+/-}$ MEFs ($n = 3$) with or without mild treatment of UCN01, a Chk1 kinase inhibitor at a very low UCN01 concentration (50 nM) that exhibits minimal effect in WT MEFs. Data are relative to WT MEFs, respectively.

*$p < 0.05$ and **$p < 0.005$, Student's t test.

See also Figure S6.

(Figure 5A), we also analyzed the PGAM/Chk1 axis in 26 human lung adenocarcinoma cells. Based on the database of Kashiwa Encyclopedia for human genome mutations in Regulatory regions and their Omics contexts (DBKERO; http://kero.hgc.jp/) (Suzuki et al., 2015), these 26 cells are classified into two subgroups; cells with genetic aberrations either in the p53 or Ras pathway (n = 14) and those with aberrations in both (n = 12) (Table S2). Then, we analyzed Pearson correlation between the levels of *Chk1* and glycolytic enzymes. Correlation coefficient between *Chk1* and most glycolytic enzymes (*HK2, GPI, ALDOA, TPI, GAPDH, PGK1, PGAM1, ENO1, and PKM1*) is high (over 0.4) in the subgroup with aberrations in both, whereas only that between *Chk1* and *TPI* is high in the former subgroup (Figures 5C, S7C and S7D).

Consistent with these implications on the significance of Ras pathway against PGAM/Chk1 axis, we noticed that PGAM-Chk1 binding is enhanced by the expression of oncogenic Ras-G12V in $p53^{-/-}$ MEFs (Figure 5D). To gain the molecular insight on the impact of Ras pathway against PGAM-Chk1 interaction, we applied several inhibitors for the downstream kinases of canonical Ras pathway in H1299; U126 (MEK inhibitor), BI-D1870 (inhibitor for ribosomal S6 kinase [RSK], a downstream kinase of MEK), and Triciribine (Akt kinase inhibitor). Although Akt inhibition unlikely affected the PGAM-Chk1 interaction (Figure S8A), the

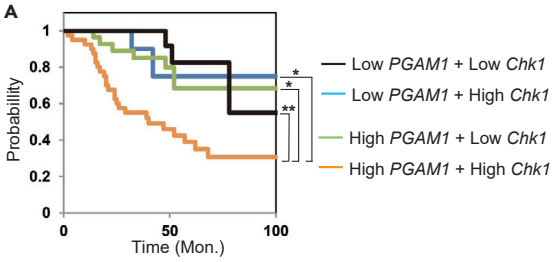

B

		siPGAM1			
		ALDO1	TPI	GAPDH	ENO1
Lung	H1299	+	++	++	++
Skin	HSC1	++	++	++	+
	HSC5	-	-	-	-
Breast	Hs578T	-	++	+	+
	MDA-MB-231	-	-	+	-
	BT474	-	+	+	+
Colon	HCT116	-	+	-	-
	RKO	-	-	-	-
	SW480	++	++	++	+
	DLD1	++	++	++	++
	HT29	-	-	-	-
Bone	SJSA-1	-	++	+	+
	U2OS	-	-	-	-
Liver	Hek293	-	-	-	-
	HepG2	-	-	-	-

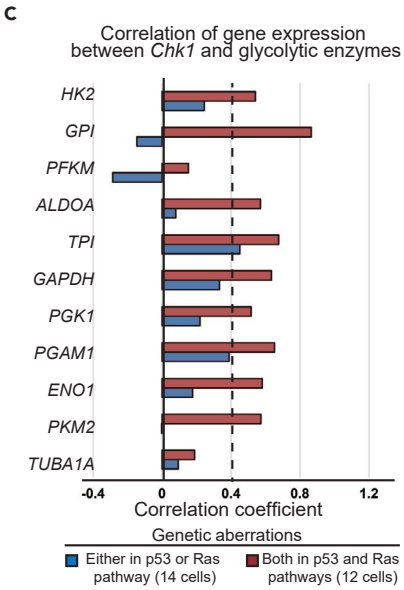

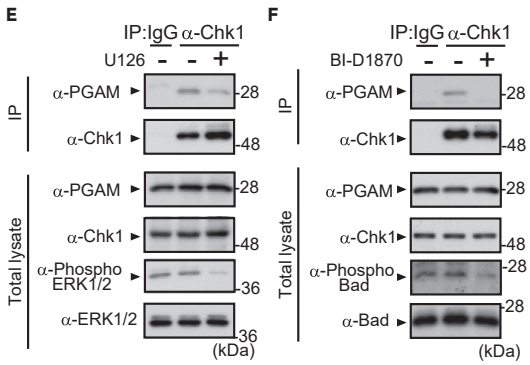

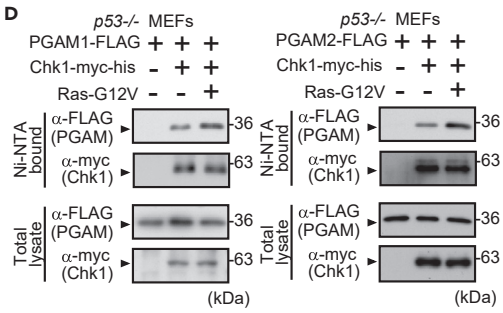

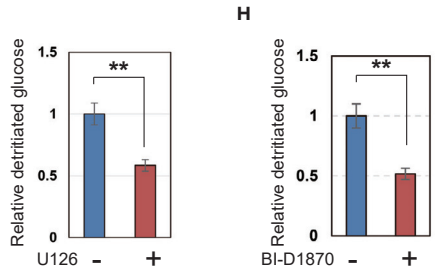

Figure 5. Oncogenic Ras Enhances PGAM-Chk1 Interaction

(A) Association between the survival and *PGAM1/Chk1* levels was analyzed in patients with non-small cell lung cancer (NSCLC) by PrognoScan database. The survivals of 104 patients with NSCLC (Dataset Jacob-00182-MSK) were plotted with Kaplan-Meier curve. Patients with NSCLC were divided into four groups: Low-*PGAM1*+Low-*Chk1* (black; n = 23), Low-*PGAM1*+High-*Chk1* (blue; n = 12), High-*PGAM1*+Low-*Chk1* (green; n = 29), and High-*PGAM1*+High-*Chk1* (orange; n = 40). *p < 0.05 and **p < 0.005, Log rank test.

(B) Summary of glycolytic mRNA downregulation by *PGAM1*-knockdown in 15 cancer cell lines tested. Original data of glycolytic mRNA expression were shown in Figure S7B. (–), <20% reduction; (+), reduction from 20 to 40%; (++), >40% reduction. *p < 0.05 and **p < 0.005, Student's t test.

(C) Summary of correlation coefficients between *Chk1* and glycolytic genes, which were evaluated in dataset of 26 NSCLC cell lines. All data were obtained from DBKERO. NSCLC cell lines were classified into two subgroups according to gene aberrations of *p53* and *Ras* pathways as shown in Table S2.

(D) The impact of Ras-G12V expression on PGAM-Chk1 binding. His-tagged protein pull-down assay was performed in indicated cells. PGAM1- or PGAM2-FLAG proteins were detected in left or right panel, respectively.

(E–H) The impact of MEK and RSK inhibition against PGAM-Chk1 interaction. H1299 cells were treated with either U126 (MEK inhibitor) or BI-D1870 (RSK inhibitor). Immunoprecipitation assay was performed to evaluate the interaction

Figure 5. *Continued*
between PGAM and Chk1 (E and F). Phosphorylation of Thr202/Tyr204 on ERK1/2 and Ser112 on Bad, which is downstream target of MEK/RSK pathway, was analyzed for assessment of U126 and BI-D1870, respectively. Glycolytic flux was measured in indicated cells (G and H).
See also Figures S7 and S8.

inactivation of MEK/RSK interferes the binding between PGAM-Chk1 (Figures 5E and 5F), followed by significant reduction in glycolytic flux (Figures 5G and 5H). Thus, oncogenic Ras signals via MEK/RSK pathway are much involved in PGAM-Chk1 interaction.

Nutlin-3a Interferes with the PGAM-Chk1 Interaction

Next, we addressed the question of whether interference with the PGAM-Chk1 interaction affects glycolysis. Nutlin-3a is a compound originally designed to inhibit the physical binding between p53 and Mdm2 (Figure S8B) (Vassilev et al., 2004). We examined the effect of Nutlin-3a on PGAM protein, as PGAM also binds Mdm2 under senescence-inducing stress (Mikawa et al., 2014). Nutlin-3a did not affect the enzymatic activity of recombinant PGAM *in vitro*, even with the increased concentrations tested (Figure S8C). Although PGAM-Mdm2 binding was not affected by Nutlin-3a (Figures 6A and S8D), Nutlin-3a treatment strikingly abolished PGAM-Chk1 binding in $p53^{-/-}$ MEFs (Figures 6B and S8E). We also treated *p53*-null H1299 cells with Nutlin-3a to disrupt PGAM-Chk1 binding to evaluate the effect on glycolytic regulation (Figure S8F). Indeed, glycolytic flux and glycolytic mRNAs in H1299 cells were downregulated by Nutlin-3a in a dose-dependent manner (Figures 6C and 6D).

Recently, the consensus sequence ([L/I/V/M]-[W/Y/F]-x-x-[L/I/V/W]) for Nutlin-3a responsive proteins, including p53, was determined by proteomic analysis (Nicholson et al., 2014). We noticed that two repeats of this consensus motif are located and conserved in the N terminus of human and mouse PGAM, which overlap with the Chk1-interacting domains (Figures 3D and 6E). PGAM mutants (*W68A* and *W78A*) with amino acid substitutions in these two repeats of the consensus sequence were generated by PCR mutagenesis (Figure 6E). Although the enzymatic activity and protein levels were maintained in both *W68A* and *W78A* mutants (Figures 6F and S8G), PGAM-Chk1 binding was largely impaired (Figures 6G and S8H). Thus, Nutlin-3a interferes with the PGAM-Chk1 interaction and the maintenance of glycolytic features but not with the enzymatic activity of PGAM.

Physical Interaction between PGAM and Chk1 Is Essential for Both Maintenance of Glycolysis and Proliferative Potential in Cancerous Cells

As PGAM mutants for Nutlin consensus motif (*W68A* and *W78A*) attenuate the interaction with Chk1 in $p53^{-/-}$ MEFs with or without Ras-G12V expression (Figures S8I and S8J), we evaluated the physiological impact of these mutants (*W68A* and *W78A*) in the conditions with or without Ras-G12V. For this purpose, Chk1-expressing $p53^{-/-}$ MEFs with or without Ras-G12V were prepared, followed by retroviral infection with various versions of PGAM. In the absence of Ras-G12V, co-expression of Chk1 with WT-, W68A-, or W78A-PGAM resulted in similar profiles for overall glycolytic mRNAs and proliferative capacity (Figures S8K, S9D, 7F, S8L, S9F, and S9G). In sharp contrast, in the presence of Ras-G12V, ectopic expression of PGAM-WT in Chk1-expressing $p53^{-/-}$ MEFs increased the glycolytic parameters (glucose consumption, glycolytic flux, and lactate production), compared with the vector control (Figures 7A–7C and S9A–S9C). Consistently, the expression of glycolytic mRNAs and proteins were upregulated in these cells (Figures 7D, 7E, S9D, and S9E). In the same genetic background, however, PGAM-W68A and W78A mutants displayed no such enhancement in glycolytic profiles (Figures 7A–7E and S9A–S9E).

Strikingly, in the presence of Ras-G12V, both the *in vitro* proliferative capacity and *in vivo* tumor growth of PGAM-WT overexpressing cells were much enhanced than control (Figures 7F–7H, S8L, and S9F–S9I). In the same genetic background, however, the cells with binding-deficient mutations (*W68A* and *W78A*) showed the similar proliferative potentials *in vitro* and *in vivo* to those in control (Figures 7F–7H, S8L, and S9F–S9I). Next, we addressed the question whether *W68A* or *W78A* mutation abolished PGAM-Chk1 binding through modulating PGAM dimerization. For this purpose, NanoLuc Binary Technology (NanoBiT) system (Promega) is applied, which enables us to quantify protein-protein interaction between the proteins with large and small NanoBiT tag (Figure S10A) (Dixon et al., 2016). We purified recombinant PGAM1, 2-WT, W68A, and W78A proteins with NanoBiT tags from the extract of bacteria (Figure S10B). We observed these recombinant PGAM proteins displayed similar intact enzymatic activity (Figure S10C). Consistently, the

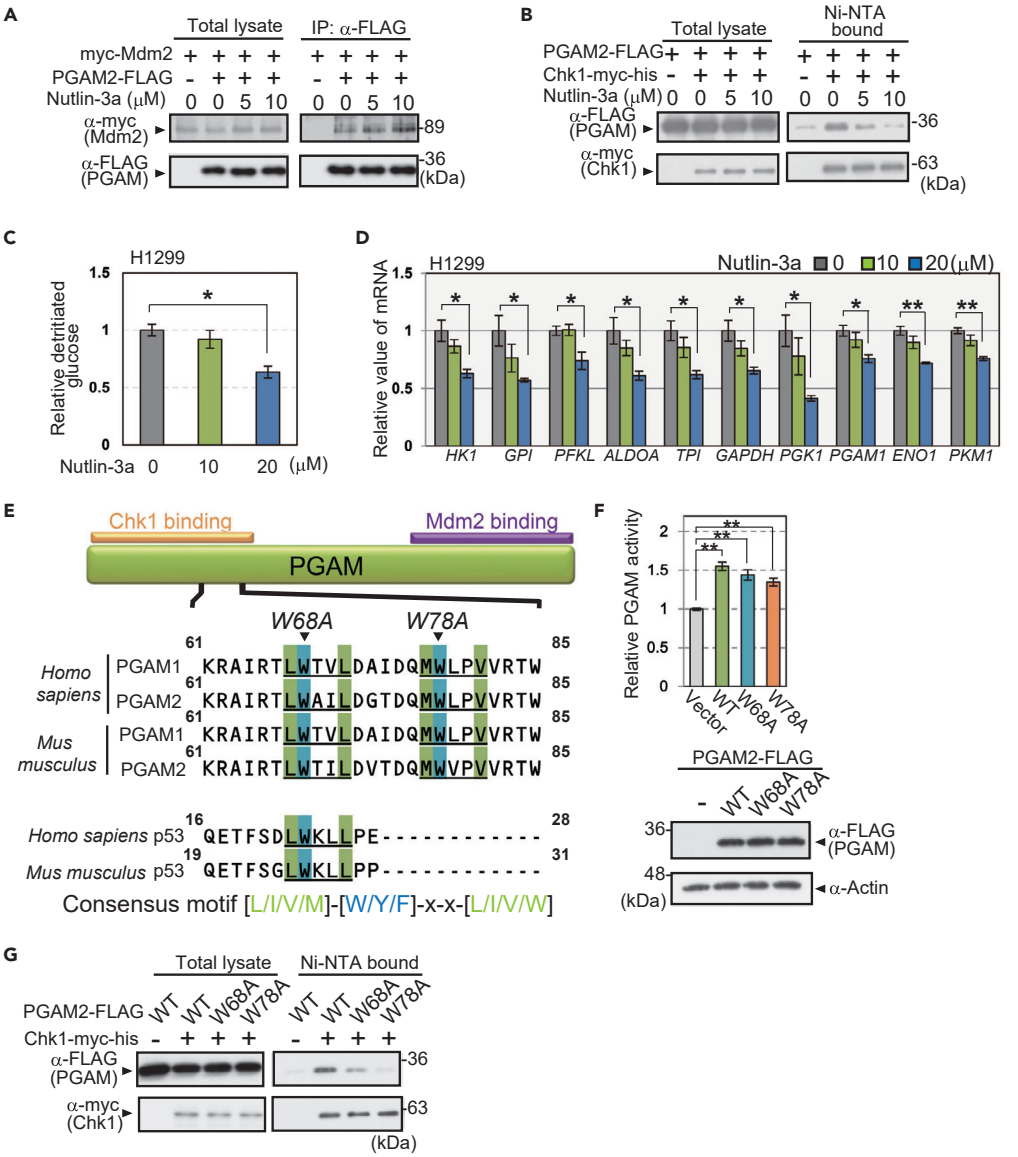

Figure 6. Cooperation of PGAM and Chk1 for Glycolytic Regulation Is Abolished by Interfering with Their Binding

(A and B) Immunoprecipitation assay or His-tagged protein pull-down assay was performed to evaluate the effect of Nutlin-3a on the interaction between PGAM and Mdm2 (A) or PGAM-Chk1 binding (B). *p53*$^{-/-}$ MEFs expressing indicated vectors were prepared. Cells were exposed to 5 or 10 μM Nutlin-3a for 48 h. After treatment with 20 μM MG132 for 3 h, cell lysates were collected. PGAM2-FLAG proteins were immunoprecipitated by anti-FLAG antibody (A) or Chk1-myc-his proteins were precipitated by Ni-NTA beads (B).

(C and D) The effect of Nutlin-3a on glycolytic profile. Comparison of glycolytic flux (C) and glycolytic mRNAs (D) among H1299 cells treated with indicated concentration of Nutlin-3a for 48 h (n = 3). Data are relative to control cells. *$p < 0.05$ and **$p < 0.005$, Dunnett's multiple comparison test.

(E) Diagram of the consensus motif of Nutlin-3-target proteins in the amino terminus of PGAM and p53. Consensus motifs, [L/I/V/M]-[W/Y/F]-x-x-[L/I/V/W], are indicated in blue and green. The alignments of the conserved consensus sequence in the amino terminus of PGAM1, 2, and p53 (human and mouse) are also presented. Orange bar, a site for Chk1 binding identified in Figure 3D. Purple bar, site for Mdm2 binding.

(F) PGAM enzymatic activity was measured in Chk1-expressing *p53*$^{-/-}$ MEFs retrovirally infected with the indicated vectors (empty vector, PGAM2-WT-FLAG, PGAM2-W68A-FLAG, and PGAM2-W78A-FLAG) (*n* = 3 each; upper panel). Protein levels for various versions of PGAM2-FLAG were shown by western blotting (lower panels). **$p < 0.005$, Dunnett's multiple comparison test.

(G) The Chk1-binding activity of PGAM2 mutants (W68A and W78A) compared with that of PGAM2-WT was analyzed with a His-tagged protein pull-down assay. Data represent the mean ± SEM.

See also Figure S8.

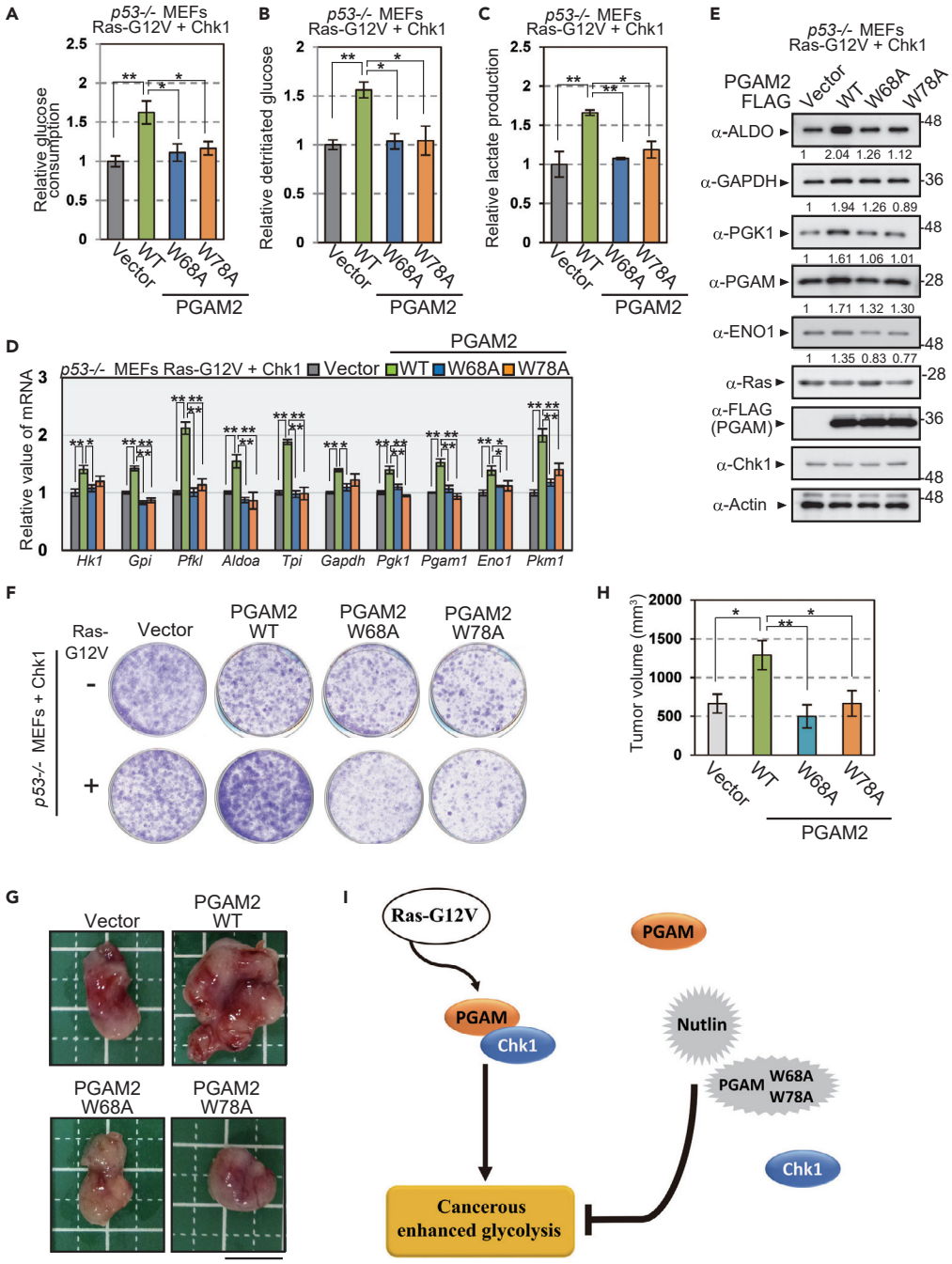

Figure 7. W68A and W78A in PGAM, Binding-Deficient Mutations with Intact Enzyme Activity, Abolished the Enhancement of Glycolytic Profiles and Proliferative Capacity in the Presence of Ras-G12V.

(A–E) Comparison of glycolytic profiles among the cells expressing PGAM2 variants (WT, W68A, or W78A) in the presence of Ras-G12V. Glucose consumption (A), glucose flux (B), and lactate production (C) were analyzed among indicated cells on the common genetic background of $p53^{-/-}$ with Ras-G12V and Chk1 ($n = 3$). The mRNA and protein levels of glycolytic enzymes were also evaluated in indicated cells (D and E). Intensity of immunoblotting bands was normalized to that of actin. Data are relative to controls expressing the empty vector.

(F) The effect of indicated PGAM2 variants on cell growth was assessed by crystal-violet staining in Chk1-expressing $p53^{-/-}$ MEFs with or without Ras-G12V.

(G and H) *In vivo* tumor growth assay in nude mice. $p53^{-/-}$ MEFs, expressing Ras-G12V, Chk1, and the indicated versions of PGAM2, were injected subcutaneously into nude mice (n = 6). (G) Representative images of tumors. (H) Measurement of

Figure 7. *Continued*
tumor volumes are shown. *p < 0.05 and **p < 0.005, Dunnett's multiple comparison test. Data represent the mean ± SEM.
(I) Schematic model on the significance of PGAM-Chk1 interaction in cancerous glycolysis. Oncogenic Ras augmented PGAM-Chk1 interaction, followed by enhanced glycolysis in cancer. Genetic or chemical ablation of the interaction abrogated such enhancement.
See also Figures S8–S11.

dimerization of either PGAM versions displayed the similar values of Kd (dissociation constant), shown by the saturation curves of NanoBiT detection; 62.5 to 67.1 nM for various versions of PGAM1 and 60.6 to 65.9 nM for those of PGAM2 (Figure S10D). Thus, PGAM-W68 and W78A did not affect dimerization and enzymatic activity of PGAM. However, we noticed that monomer forms of PGAM were much abundant in H1299 cancer cells, compared with those in standard WI-38 cells (Figure S10E). These findings support the possibility that nonenzymatic PGAM is more accumulated in cancer cells.

Finally, we evaluated the impact of enzymatic PGAM mutants in the same setting. As the patients with PGAM deficiency were previously reported (Naini et al., 2009), the point mutation *R90W* in the patients abolished PGAM enzymatic activity (Tsujino et al., 1995). We generated cDNA clone of PGAM1 and 2 with *R90W* mutation. We observed that such mutation in both PGAM isoforms abolished PGAM activity (Figures S11A and S11B) but still retains proliferative advantage compared with vector control, in Chk1 and Ras-G12V-expressing $p53^{-/-}$ MEFs (Figures S11C and S11D).

Thus, in accordance with the observation of chemically interfering by Nutlin, the genetical interference of PGAM-Chk1 binding with intact PGAM activity (*W68A*, *W78A* mutations) abolished cancerous proliferation and enhanced glycolytic profiles, in the presence of oncogenic Ras (Figure 7I).

DISCUSSION

Here we demonstrated a previously unappreciated regulatory mechanism for cancerous glycolysis via the PGAM-Chk1 interaction. Genetic and chemical dissection for its interaction disclosed a "non-enzymatic" role for PGAM, especially under oncogenic Ras expressing conditions. Thus, we unveiled the noteworthy impact of interfering with the PGAM/Chk1 axis in the cancerous glycolysis.

First, our data indicate the evident genetic link between PGAM and the global enhancement of glycolytic profiles frequently observed in cancerous cells. We found a molecular interaction between PGAM and Chk1 as notable glycolytic regulator, which is operating in cancer cells, not in standard cells. Moreover, in addition to the data on the prognosis of patients with cancer, several close correlations between Chk1/PGAM and glycolytic enzymes identified oncogenic Ras mutations, which are highly prevalent both in human cancers and DMBA-treated tissues (Karnoub and Weinberg, 2008), as enhancer of PGAM-Chk1 interaction. Although the other research has also emphasized the distinct impact of PGAM in cancer metabolism (Evans et al., 2005; Vander Heiden et al., 2010), we identified the essential effect of PGAM on the boost of glycolysis in the cancerous conditions.

Second, our study also disclosed the key metabolic role of Chk1 for glycolytic regulation in cancer. Chk1, initially identified as a checkpoint kinase, was known to induce cell-cycle arrest after its activation during DNA damage or senescence-inducing stress (Sancar et al., 2004). Other studies, however, have suggested the opposing notions that Chk1 would be the critical driver of cellular proliferation in ES cells and cancer cells *in vitro* (Liu et al., 2000; Shimada et al., 2008) and in carcinogenic events *in vivo* (Tho et al., 2012). Interestingly, Chk1 was reported to be regulated by RSK, the downstream kinase of Ras pathway, during cell cycle progression (Li et al., 2012). RSK is upregulated in many types of cancer including lung cancer and promotes cancerous proliferation (Houles and Roux, 2018), whose impacts on the Warburg effect were scarcely reported. As our findings suggest that oncogenic Ras/RSK activation are closely involved in PGAM-Chk1 binding, the opposing roles of Chk1 with respect to cell proliferation would be cellular-context dependent, including the modulation of Ras/RSK pathway.

Third, our findings in the binding-deficient mutants of PGAM implicate that regardless of its enzymatic activity, PGAM plays a critical role in the regulation of glycolytic upregulation. Although neither the phosphatase nor enzymatic activity of PGAM was found to be required for the functional cooperation with Chk1, the physical interaction between PGAM and Chk1 is essential for glycolytic upregulation. These findings are

rather consistent with the previous notion that the multifaceted roles of some enzymes are independent of their catalytic activity (Mdm2 for Poyurovsky et al. [2003]; PP2A for Takemoto et al. [2009]). It is possible that in cancerous cells with accumulation of PGAM proteins, "nonenzymatic" PGAM cooperates with the Chk1 pathway to boost glycolysis, whose activation is required for the survival of cancers bearing oncogenic Ras mutation (Dietlein et al., 2015). A plausible explanation for the Warburg effect has been proposed as follows: besides hypoxic adaptation, it might not only enable cancer cells to meet demands both for energy and biosynthesis (Lunt and Vander Heiden, 2011) but also protect them from oxidative damages (Kondoh et al., 2007). Interestingly, the recent studies suggested that PGAM interacts with actin proteins as nonenzymatic role, to facilitate cancer motility (Huang et al., 2019; Zhang et al., 2017). In addition to the above, the identification of nonenzymatic role for PGAM suggested that enhanced glycolysis might support proliferative capacity of rapidly dividing cells through the cooperation with Chk1.

Finally, our analysis also supported the clinical significance of PGAM-Chk1 interaction. Nutlin-3a, an anticancer drug as inhibitor of p53-Mdm2 binding (Burgess et al., 2016), interfered with the PGAM-Chk1 interaction in a p53-independent manner but not with PGAM enzymatic activity. Thus, Nutlin-3a likely also functions as a glycolytic modulator through interfering with the PGAM-Chk1 interaction. Since the discovery of the Warburg effect, cancer metabolism has long been assumed to be a potential anticancer therapeutic target. However, enzymatic inhibition of glycolysis has failed in clinical trials as anticancer drugs owing to their profound adverse effects (Granchi and Minutolo, 2012). Therefore, targeting the binding between PGAM and Chk1 would represent a potential candidate strategy for anti-cancer therapy.

Limitation of the Study

Skin carcinogenesis protocol was performed in *Pgam2-Tg* mice, whereas *in vivo* tumor formation assay in nude mice was performed in PGAM1- or PGAM2-expressing cells. In the future, it would be worthy to explore the PGAM/Chk1 axis in human clinical samples.

Resource Availability

Lead Contact

Further information and requests for resources and reagents should be directed to and will be fulfilled by the Lead Contact, Dr.Hiroshi Kondoh, hkondoh@kuhp.kyoto-u.ac.jp.

Materials Availability

All unique reagents generated in this study are available on reasonable request with a completed Materials Transfer Agreement.

Data and Code Availability

All data are available in the main text or the Supplemental Information.

METHODS

All methods can be found in the accompanying Transparent Methods supplemental file.

SUPPLEMENTAL INFORMATION

Supplemental Information can be found online at https://doi.org/10.1016/j.isci.2020.101306.

ACKNOWLEDGMENTS

We thank all the staff of Geriatric unit and of the Department of Diabetes, Endocrinology and Nutrition at Kyoto University for their cooperation; Dr. Kayoko Maehara for the pBabe-puro-Ras-G12V vector; Dr. Toshio Kitamura for the PLAT-A cells. This work was supported in part by grants from the Japan Society for the Promotion of Science, Japan (Grants No. 26310103 and No. 15K19283) and by the Japan Agency for Medical Research and Development (AMED), Japan, Core Research for Evolutional Science and Technology, Japan (CREST JP17gm0610002h0306). The animal experiments and radio-isotope experiments were performed at the Institute of Laboratory Animals, Graduate School of Medicine, Kyoto University, and in the Kyoto University Hospital Radioisotopes Research Laboratory, respectively.

AUTHOR CONTRIBUTIONS

T.M., E.S., M.S., K.I., T.I., H. Kanda, K.T., and M.E.L. researched and analyzed the data. N.I. and M.Y. provided technical support and contributed to discussions. H. Kondoh wrote the paper and supervised this study. All the authors read and approved the manuscript.

DECLARATION OF INTERESTS

T.M. and H. Kondoh have submitted relevant patent on the impact of PGAM-Chk1 for glycolysis.

Received: January 15, 2020
Revised: May 20, 2020
Accepted: June 18, 2020
Published: July 24, 2020

REFERENCES

Ahn, J.Y., Schwarz, J.K., Piwnica-Worms, H., and Canman, C.E. (2000). Threonine 68 phosphorylation by ataxia telangiectasia mutated is required for efficient activation of Chk2 in response to ionizing radiation. Cancer Res. *60*, 5934–5936.

Bensaad, K., and Vousden, K.H. (2007). p53: new roles in metabolism. Trends Cell Biol. *17*, 286–291.

Burgess, A., Chia, K.M., Haupt, S., Thomas, D., Haupt, Y., and Lim, E. (2016). Clinical overview of MDM2/X-targeted therapies. Front. Oncol. *6*, 7.

Cancer Genome Atlas Research, N. (2008). Comprehensive genomic characterization defines human glioblastoma genes and core pathways. Nature *455*, 1061–1068.

Chimenti, M.S., Triggianese, P., Conigliaro, P., Candi, E., Melino, G., and Perricone, R. (2015). The interplay between inflammation and metabolism in rheumatoid arthritis. Cell Death Dis. *6*, e1887.

Dang, C.V., and Semenza, G.L. (1999). Oncogenic alterations of metabolism. Trends Biochem. Sci. *24*, 68–72.

Di Micco, R., Fumagalli, M., Cicalese, A., Piccinin, S., Gasparini, P., Luise, C., Schurra, C., Garre, M., Nuciforo, P.G., Bensimon, A., et al. (2006). Oncogene-induced senescence is a DNA damage response triggered by DNA hyper-replication. Nature *444*, 638–642.

Dietlein, F., Kalb, B., Jokic, M., Noll, E.M., Strong, A., Tharun, L., Ozretic, L., Kunstlinger, H., Kambartel, K., Randerath, W.J., et al. (2015). A synergistic interaction between Chk1- and MK2 inhibitors in KRAS-mutant cancer. Cell *162*, 146–159.

Director's Challenge Consortium for the Molecular Classification of Lung Adenocarcinoma, Shedden, K., Taylor, J.M., Enkemann, S.A., Tsao, M.S., Yeatman, T.J., Gerald, W.L., Eschrich, S., Jurisica, I., Giordano, T.J., et al. (2008). Gene expression-based survival prediction in lung adenocarcinoma: a multi-site, blinded validation study. Nat. Med. *14*, 822–827.

Dixon, A.S., Schwinn, M.K., Hall, M.P., Zimmerman, K., Otto, P., Lubben, T.H., Butler, B.L., Binkowski, B.F., Machleidt, T., Kirkland, T.A., et al. (2016). NanoLuc complementation reporter optimized for accurate measurement of protein interactions in cells. ACS Chem. Biol. *11*, 400–408.

Durany, N., Joseph, J., Campo, E., Molina, R., and Carreras, J. (1997). Phosphoglycerate mutase, 2,3-bisphosphoglycerate phosphatase and enolase activity and isoenzymes in lung, colon and liver carcinomas. Br. J. Cancer *75*, 969–977.

Evans, M.J., Saghatelian, A., Sorensen, E.J., and Cravatt, B.F. (2005). Target discovery in small-molecule cell-based screens by in situ proteome reactivity profiling. Nat. Biotechnol. *23*, 1303–1307.

Fujii, K., Dousaka-Nakajima, N., and Imamura, S. (1995). Epidermal growth factor enhancement of HSC-1 human cutaneous squamous carcinoma cell adhesion and migration on type I collagen involves selective up-regulation of alpha 2 beta 1 integrin expression. Exp. Cell Res. *216*, 261–272.

Goyal, M.S., Vlassenko, A.G., Blazey, T.M., Su, Y., Couture, L.E., Durbin, T.J., Bateman, R.J., Benzinger, T.L., Morris, J.C., and Raichle, M.E. (2017). Loss of brain aerobic glycolysis in normal human aging. Cell Metab *26*, 353–360.e3.

Granchi, C., and Minutolo, F. (2012). Anticancer agents that counteract tumor glycolysis. ChemMedChem *7*, 1318–1350.

Hitosugi, T., Zhou, L., Elf, S., Fan, J., Kang, H.B., Seo, J.H., Shan, C., Dai, Q., Zhang, L., Xie, J., et al. (2012). Phosphoglycerate mutase 1 coordinates glycolysis and biosynthesis to promote tumor growth. Cancer Cell *22*, 585–600.

Hori, M., Suzuki, K., Udono, M.U., Yamauchi, M., Mine, M., Watanabe, M., Kondo, S., and Hozumi, Y. (2009). Establishment of ponasterone A-inducible the wild-type p53 protein-expressing clones from HSC-1 cells, cell growth suppression by p53 expression and the suppression mechanism. Arch. Dermatol. Res. *301*, 631–646.

Houles, T., and Roux, P.P. (2018). Defining the role of the RSK isoforms in cancer. Semin. Cancer Biol. *48*, 53–61.

Huang, K., Liang, Q., Zhou, Y., Jiang, L.L., Gu, W.M., Luo, M.Y., Tang, Y.B., Wang, Y., Lu, W., Huang, M., et al. (2019). A novel allosteric inhibitor of phosphoglycerate mutase 1 suppresses growth and metastasis of non-small-cell lung cancer. Cell Metab. *30*, 1107–1119.e8.

Karnoub, A.E., and Weinberg, R.A. (2008). Ras oncogenes: split personalities. Nat. Rev. Mol. Cell Biol. *9*, 517–531.

Klijn, C., Durinck, S., Stawiski, E.W., Haverty, P.M., Jiang, Z., Liu, H., Degenhardt, J., Mayba, O., Gnad, F., Liu, J., et al. (2015). A comprehensive transcriptional portrait of human cancer cell lines. Nat. Biotechnol. *33*, 306–312.

Kondoh, H., Lleonart, M.E., Gil, J., Wang, J., Degan, P., Peters, G., Martinez, D., Carnero, A., and Beach, D. (2005). Glycolytic enzymes can modulate cellular life span. Cancer Res. *65*, 177–185.

Kondoh, H., Lleonart, M.E., Nakashima, Y., Yokode, M., Tanaka, M., Bernard, D., Gil, J., and Beach, D. (2007). A high glycolytic flux supports the proliferative potential of murine embryonic stem cells. Antioxid. Redox Signal. *9*, 293–299.

Koppenol, W.H., Bounds, P.L., and Dang, C.V. (2011). Otto Warburg's contributions to current concepts of cancer metabolism. Nat. Rev. Cancer *11*, 325–337.

Li, P., Goto, H., Kasahara, K., Matsuyama, M., Wang, Z., Yatabe, Y., Kiyono, T., and Inagaki, M. (2012). P90 RSK arranges Chk1 in the nucleus for monitoring of genomic integrity during cell proliferation. Mol. Biol. Cell *23*, 1582–1592.

Liu, Q., Guntuku, S., Cui, X.S., Matsuoka, S., Cortez, D., Tamai, K., Luo, G., Carattini-Rivera, S., DeMayo, F., Bradley, A., et al. (2000). Chk1 is an essential kinase that is regulated by Atr and required for the G(2)/M DNA damage checkpoint. Genes Dev. *14*, 1448–1459.

Lunt, S.Y., and Vander Heiden, M.G. (2011). Aerobic glycolysis: meeting the metabolic requirements of cell proliferation. Annu. Rev. Cell Dev Biol. *27*, 441–464.

Mikawa, T., Maruyama, T., Okamoto, K., Nakagama, H., Lleonart, M.E., Tsusaka, T., Hori, K., Murakami, I., Izumi, T., Takaori-Kondo, A., et al. (2014). Senescence-inducing stress promotes proteolysis of phosphoglycerate mutase via ubiquitin ligase Mdm2. J. Cell Biol. *204*, 729–745.

Mikawa, T., ME, L.L., Takaori-Kondo, A., Inagaki, N., Yokode, M., and Kondoh, H. (2015). Dysregulated glycolysis as an oncogenic event. Cell Mol. Life Sci. *72*, 1881–1892.

Mizuno, H., Kitada, K., Nakai, K., and Sarai, A. (2009). PrognoScan: a new database for meta-analysis of the prognostic value of genes. BMC Med. Genomics *2*, 18.

Naini, A., Toscano, A., Musumeci, O., Vissing, J., Akman, H.O., and DiMauro, S. (2009). Muscle phosphoglycerate mutase deficiency revisited. Arch. Neurol. *66*, 394–398.

Nicholson, J., Scherl, A., Way, L., Blackburn, E.A., Walkinshaw, M.D., Ball, K.L., and Hupp, T.R. (2014). A systems wide mass spectrometric based linear motif screen to identify dominant in-vivo interacting proteins for the ubiquitin ligase MDM2. Cell Signal. *26*, 1243–1257.

Okuda, J., Niizuma, S., Shioi, T., Kato, T., Inuzuka, Y., Kawashima, T., Tamaki, Y., Kawamoto, A., Tanada, Y., Iwanaga, Y., et al. (2013). Persistent overexpression of phosphoglycerate mutase, a glycolytic enzyme, modifies energy metabolism and reduces stress resistance of heart in mice. PLoS One *8*, e72173.

Oliner, J.D., Kinzler, K.W., Meltzer, P.S., George, D.L., and Vogelstein, B. (1992). Amplification of a gene encoding a p53-associated protein in human sarcomas. Nature *358*, 80–83.

Poyurovsky, M.V., Jacq, X., Ma, C., Karni-Schmidt, O., Parker, P.J., Chalfie, M., Manley, J.L., and Prives, C. (2003). Nucleotide binding by the Mdm2 RING domain facilitates Arf-independent Mdm2 nucleolar localization. Mol. Cell *12*, 875–887.

Rodwell, V.W., Towne, J.C., and Grisolia, S. (1957). The kinetic properties of yeast and muscle phosphoglyceric acid mutase. J. Biol. Chem. *228*, 875–890.

Sancar, A., Lindsey-Boltz, L.A., Unsal-Kacmaz, K., and Linn, S. (2004). Molecular mechanisms of mammalian DNA repair and the DNA damage checkpoints. Annu. Rev. Biochem. *73*, 39–85.

Shieh, S.Y., Ahn, J., Tamai, K., Taya, Y., and Prives, C. (2000). The human homologs of checkpoint kinases Chk1 and Cds1 (Chk2) phosphorylate p53 at multiple DNA damage-inducible sites. Genes Dev. *14*, 289–300.

Shimada, M., Niida, H., Zineldeen, D.H., Tagami, H., Tanaka, M., Saito, H., and Nakanishi, M. (2008). Chk1 is a histone H3 threonine 11 kinase that regulates DNA damage-induced transcriptional repression. Cell *132*, 221–232.

Suzuki, A., Wakaguri, H., Yamashita, R., Kawano, S., Tsuchihara, K., Sugano, S., Suzuki, Y., and Nakai, K. (2015). DBTSS as an integrative platform for transcriptome, epigenome and genome sequence variation data. Nucleic Acids Res. *43*, D87–D91.

Takemoto, A., Maeshima, K., Ikehara, T., Yamaguchi, K., Murayama, A., Imamura, S., Imamoto, N., Yokoyama, S., Hirano, T., Watanabe, Y., et al. (2009). The chromosomal association of condensin II is regulated by a noncatalytic function of PP2A. Nat. Struct. Mol. Biol. *16*, 1302–1308.

Taylor, M., Wallhaus, T.R., Degrado, T.R., Russell, D.C., Stanko, P., Nickles, R.J., and Stone, C.K. (2001). An evaluation of myocardial fatty acid and glucose uptake using PET with [18F]fluoro-6-thia-heptadecanoic acid and [18F]FDG in Patients with Congestive Heart Failure. J. Nucl. Med. *42*, 55–62.

Tho, L.M., Libertini, S., Rampling, R., Sansom, O., and Gillespie, D.A. (2012). Chk1 is essential for chemical carcinogen-induced mouse skin tumorigenesis. Oncogene *31*, 1366–1375.

Tsongalis, G.J., Peterson, J.D., de Abreu, F.B., Tunkey, C.D., Gallagher, T.L., Strausbaugh, L.D., Wells, W.A., and Amos, C.I. (2014). Routine use of the Ion Torrent AmpliSeq cancer Hotspot panel for identification of clinically actionable somatic mutations. Clin. Chem. Lab. Med. *52*, 707–714.

Tsujino, S., Shanske, S., Sakoda, S., Toscano, A., and DiMauro, S. (1995). Molecular genetic studies in muscle phosphoglycerate mutase (PGAM-M) deficiency. Muscle Nerve Suppl. *3*, S50–S53.

Vander Heiden, M.G., Cantley, L.C., and Thompson, C.B. (2009). Understanding the Warburg effect: the metabolic requirements of cell proliferation. Science *324*, 1029–1033.

Vander Heiden, M.G., Locasale, J.W., Swanson, K.D., Sharfi, H., Heffron, G.J., Amador-Noguez, D., Christofk, H.R., Wagner, G., Rabinowitz, J.D., Asara, J.M., et al. (2010). Evidence for an alternative glycolytic pathway in rapidly proliferating cells. Science *329*, 1492–1499.

Vassilev, L.T., Vu, B.T., Graves, B., Carvajal, D., Podlaski, F., Filipovic, Z., Kong, N., Kammlott, U., Lukacs, C., Klein, C., et al. (2004). In vivo activation of the p53 pathway by small-molecule antagonists of MDM2. Science *303*, 844–848.

Wang, Y., Cai, W.S., Chen, L., and Wang, G. (2017). Molecular dynamics simulation reveals how phosphorylation of tyrosine 26 of phosphoglycerate mutase 1 upregulates glycolysis and promotes tumor growth. Oncotarget *8*, 12093–12107.

Warburg, O. (1956). On respiratory impairment in cancer cells. Science *124*, 269–270.

White, M.F., and Fothergill-Gilmore, L.A. (1992). Development of a mutagenesis, expression and purification system for yeast phosphoglycerate mutase. Investigation of the role of active-site His181. Eur. J. Biochem. *207*, 709–714.

Xu, Y., Li, F., Lv, L., Li, T., Zhou, X., Deng, C.X., Guan, K.L., Lei, Q.Y., and Xiong, Y. (2014). Oxidative stress activates SIRT2 to deacetylate and stimulate phosphoglycerate mutase. Cancer Res. *74*, 3630–3642.

Zhang, D., Jin, N., Sun, W., Li, X., Liu, B., Xie, Z., Qu, J., Xu, J., Yang, X., Su, Y., et al. (2017). Phosphoglycerate mutase 1 promotes cancer cell migration independent of its metabolic activity. Oncogene *36*, 2900–2909.

Zhang, J., Yu, L., Fu, Q., Gao, J., Xie, Y., Chen, J., Zhang, P., Liu, Q., and Zhao, S. (2001). Mouse phosphoglycerate mutase M and B isozymes: cDNA cloning, enzyme activity assay and mapping. Gene *264*, 273–279.

Zhao, H., and Piwnica-Worms, H. (2001). ATR-mediated checkpoint pathways regulate phosphorylation and activation of human Chk1. Mol. Cell. Biol. *21*, 4129–4139.

iScience, Volume *23*

Supplemental Information

Phosphoglycerate Mutase Cooperates with Chk1 Kinase to Regulate Glycolysis

Takumi Mikawa, Eri Shibata, Midori Shimada, Ken Ito, Tomiko Ito, Hiroaki Kanda, Keiyo Takubo, Matilde E. Lleonart, Nobuya Inagaki, Masayuki Yokode, and Hiroshi Kondoh

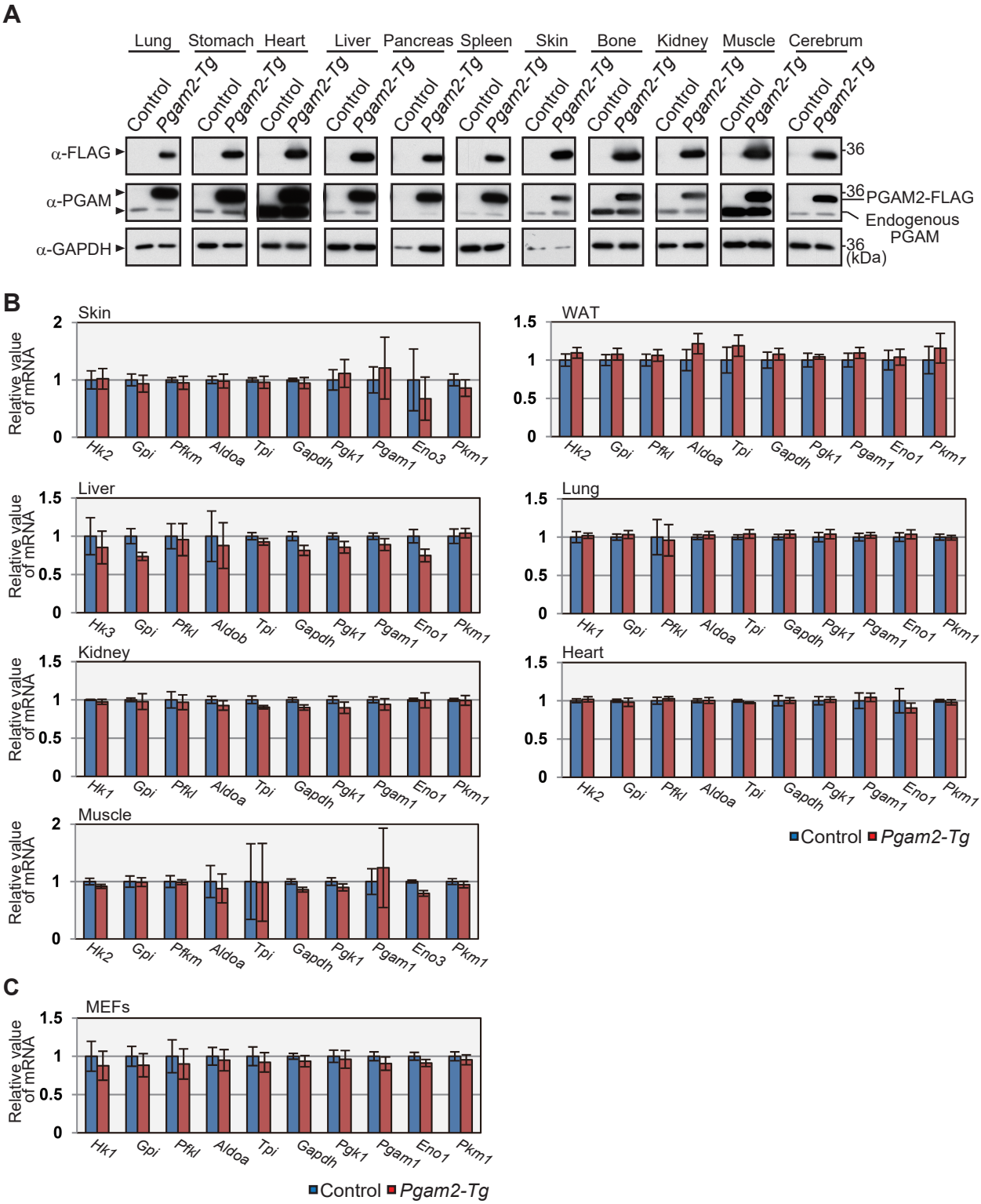
A
Lung
Stomach
Heart
Liver
Pancreas
Spleen
Skin
Bone
Kidney
Muscle
Cerebrum
Control
Pgam2-Tg
α-FLAG
α-PGAM
α-GAPDH
36
PGAM2-FLAG
Endogenous PGAM
(kDa)
B
Skin
WAT
Liver
Lung
Kidney
Heart
Muscle
Relative value of mRNA
Hk2 Gpi Pfkm Aldoa Tpi Gapdh Pgk1 Pgam1 Eno3 Pkm1
Hk2 Gpi Pfkl Aldoa Tpi Gapdh Pgk1 Pgam1 Eno1 Pkm1
Hk3 Gpi Pfkl Aldob Tpi Gapdh Pgk1 Pgam1 Eno1 Pkm1
Hk1 Gpi Pfkl Aldoa Tpi Gapdh Pgk1 Pgam1 Eno1 Pkm1
Hk2 Gpi Pfkm Aldoa Tpi Gapdh Pgk1 Pgam1 Eno3 Pkm1
Control
Pgam2-Tg
C
MEFs
Hk1 Gpi Pfkl Aldoa Tpi Gapdh Pgk1 Pgam1 Eno1 Pkm1
Control
Pgam2-Tg

Figure S1. Glycolytic profiles in *Pgam2-Tg* mice. Related to Figure 1

(A) Ectopic expression of PGAM2-FLAG was detected by immunoblotting in various tissues from control (wild-type) and *Pgam2-Tg* mice. Anti-FLAG, anti-PGAM, and anti-GAPDH antibodies were used. **(B)** Relative mRNA levels for glycolytic enzymes in control (WT; *n* = 4) and *Pgam2-Tg* (*n* = 4) mice. Total RNA was extracted from various tissues, including skin, liver, kidney, muscle, white adipose tissue (WAT), lung, and heart. **(C)** Relative mRNA levels for glycolytic enzymes in control (*n* = 3) and *Pgam2-Tg* MEFs (*n* = 3). Data are relative to those expressed in control. *Hk1*: hexokinase1; *Hk2*: hexokinase2; *Hk3*: hexokinase3; *Gpi*: glucose phosphate isomerase; *Pfkl*: phosphofructokinase L; *Pfkm*: phosphofructokinase M; *Aldoa*: aldolase A; *Aldob*: aldolase B;*Tpi*: triose phosphate isomerase; *Gapdh*: glyceraldehyde 3-phosphate dehydrogenase; *Pgk1*: phosphoglycerate kinase1; *Pgam1*: phosphoglycerate mutase1;*Eno1*: enolase1; *Eno3*: enolase3; *Pkm1*: pyruvate kinase M1.

A

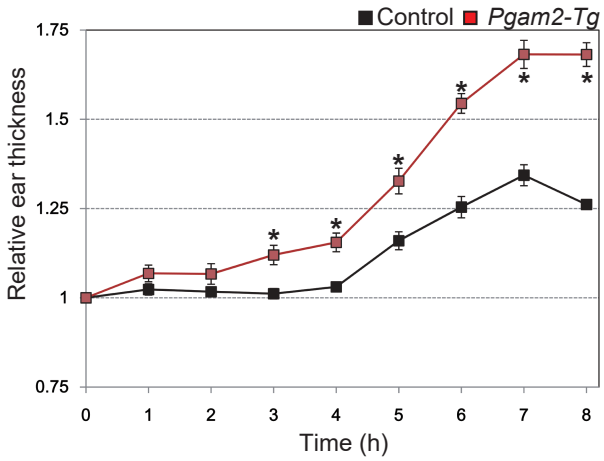
Control
Pgam2-Tg
Relative ear thickness
1.75
1.5
1.25
1
0.75
0
1
2
3
4
5
6
7
8
Time (h)
*

B


Control
Pgam2-Tg

C

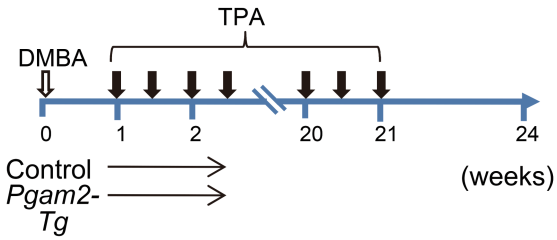
TPA
DMBA
0
1
2
20
21
24
Control
Pgam2-Tg
(weeks)

D

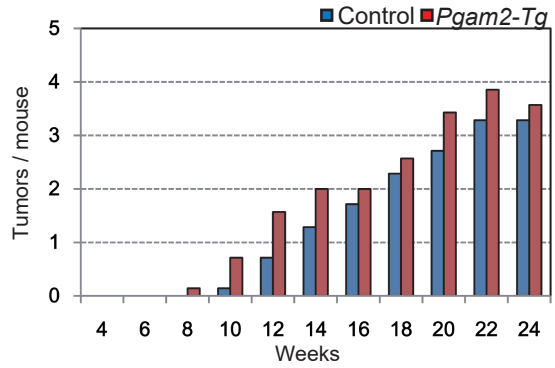
Control
Pgam2-Tg
Tumors / mouse
5
4
3
2
1
0
4
6
8
10
12
14
16
18
20
22
24
Weeks

Figure S2. TPA-induced skin inflammation and chemically induced tumorigenesis in *Pgam2-Tg* mice. Related to Figure 1

(A-B) Comparison of proinflammatory TPA-treated ears between control (wild-type) (n=3) and *Pgam2-Tg* mice (n=3). **(A)** Mice at 35 weeks were treated with 10 ng TPA on the ears whose thickness were monitored for 8 hours. **(B)** Representative pictures of TPA-treated ears in control and *Pgam2-Tg* mice. **P*<0.05, Student's t-test. Data represent the mean ± SEM. **(C)** Schematic of the chemically-induced skin tumorigenesis protocol. Mice were treated with DMBA on Day 0, followed by treatment with TPA twice a week for 20 weeks. Histological examination of tumors was performed at 24 weeks. **(D)** Summary of total tumors during the protocol.

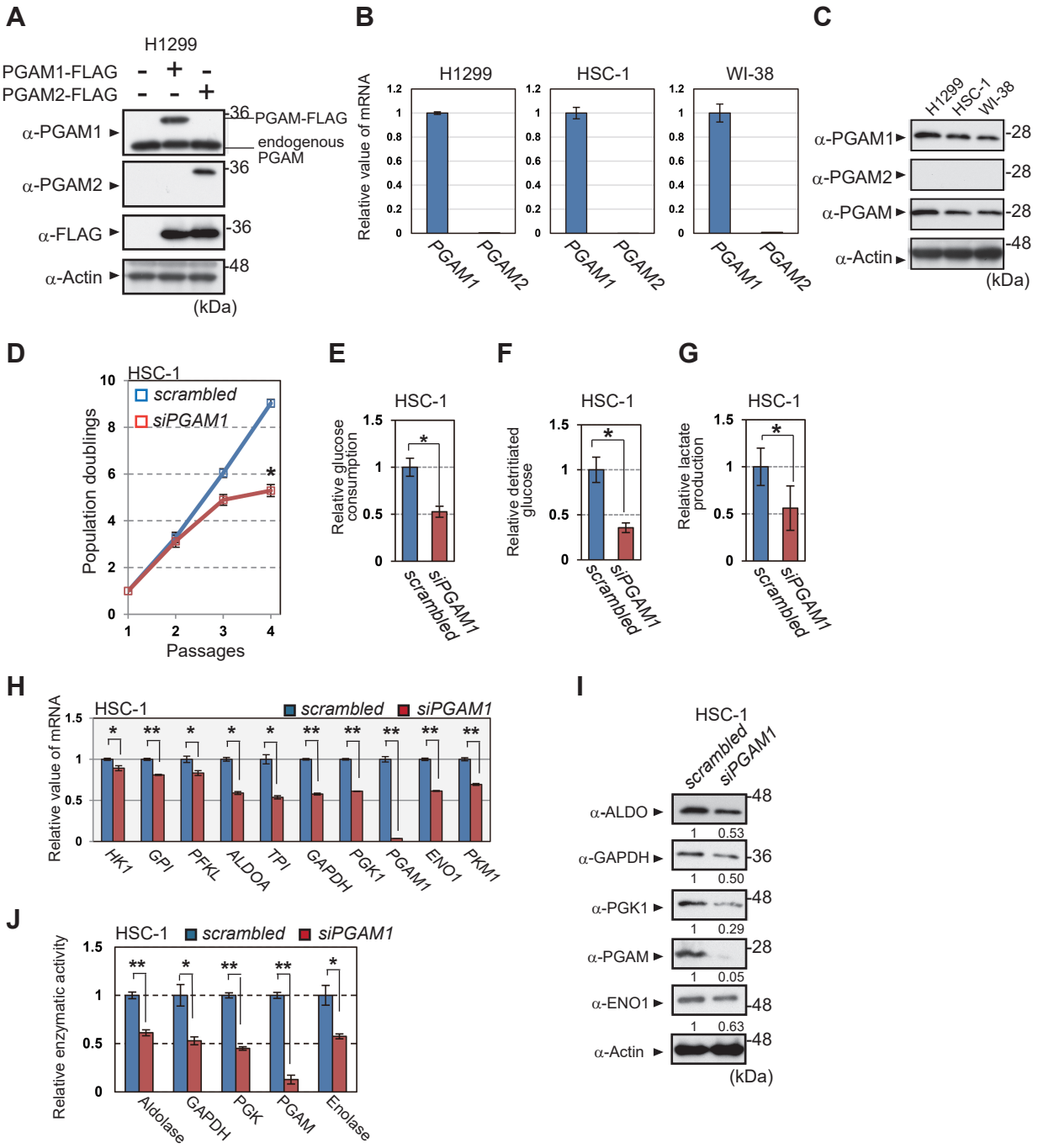
A
H1299
PGAM1-FLAG - + -
PGAM2-FLAG - - +
α-PGAM1
α-PGAM2
α-FLAG
α-Actin
36
PGAM-FLAG
endogenous PGAM
36
36
48
(kDa)
B
H1299
HSC-1
WI-38
Relative value of mRNA
PGAM1
PGAM2
C
H1299
HSC-1
WI-38
α-PGAM1
α-PGAM2
α-PGAM
α-Actin
28
28
28
48
(kDa)
D
HSC-1
scrambled
siPGAM1
Population doublings
Passages
E
HSC-1
Relative glucose consumption
siPGAM1
scrambled
F
HSC-1
Relative detritiated glucose
siPGAM1
scrambled
G
HSC-1
Relative lactate production
siPGAM1
scrambled
H
HSC-1
scrambled
siPGAM1
Relative value of mRNA
HK1
GPI
PFKL
ALDOA
TPI
GAPDH
PGK1
PGAM1
ENO1
PKM1
I
HSC-1
scrambled
siPGAM1
α-ALDO
α-GAPDH
α-PGK1
α-PGAM
α-ENO1
α-Actin
48
1 0.53
36
1 0.50
48
1 0.29
28
1 0.05
48
1 0.63
48
(kDa)
J
HSC-1
scrambled
siPGAM1
Relative enzymatic activity
Aldolase
GAPDH
PGK
PGAM
Enolase

Figure S3. Abrogation of PGAM inHSC-1 cells. Related to Figure 2

(A-C) The profiles of PGAM isoforms in H1299, HSC-1, and WI-38 cells. **(A)** Validation of antibodies against PGAM1 and 2. Western blotting was performed using the extracts from the transfected cells with indicated plasmids. Antibodies against PGAM1 (Abcam, ab129191) or PGAM2 (Abcam, ab183027) were applied. **(B)** The mRNA profiles of PGAM isoforms in indicated cells were evaluated by RT-PCR. **(C)** The protein profiles of PGAM isoforms in indicated cells. Anti PGAM antibody detects both isoforms, while anti PGAM1 or PGAM2 antibody detects relevant isoforms, as shown in panel (A). **(D-J)** The impact of *PGAM1* knockdown in HSC-1 cells *in vitro*. HSC-1 cells were transfected with *siPGAM1* (n=3) or scrambled RNA (n=3). **(D)** The proliferation curves of *PGAM1*-knockdown HSC-1 cells. Cells were passaged according to 3T3 cell culture protocol. **(E-I)** The glycolytic profiles were evaluated in *PGAM1*-knockdown HSC-1 cells. Glucose consumption was evaluated by measuring glucose concentration in medium **(E)**, whereas glycolytic flux was evaluated using ^{3}H-labeled glucose **(F)**. Lactate production was determined by the measurements of lactate concentration in medium **(G)**. **(H and I)** The mRNA and protein levels for glycolytic enzymes were assessed. The protein levels of the indicated glycolytic enzymes were analyzed by immunoblot (I). **(J)** Enzymatic activity of aldolase, GAPDH, PGK, PGAM and enolase was measured by spectrometric assay. *P < 0.05 and **P < 0.005, Student's t-test.

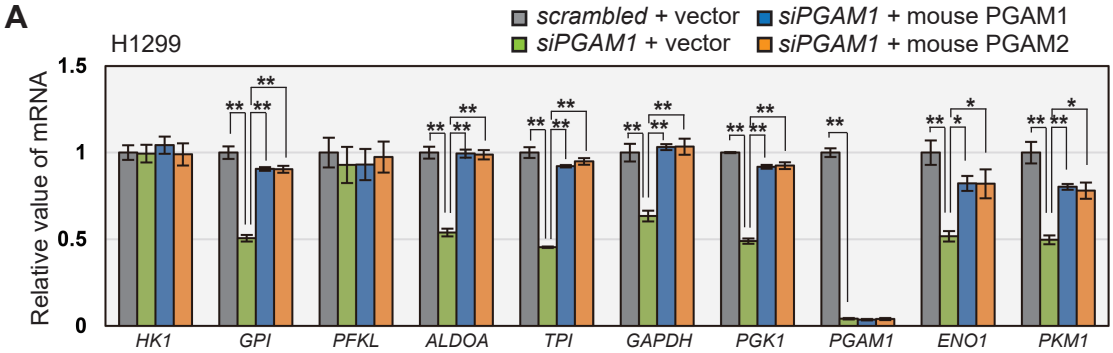
A
H1299
scrambled + vector
siPGAM1 + vector
siPGAM1 + mouse PGAM1
siPGAM1 + mouse PGAM2
Relative value of mRNA
HK1
GPI
PFKL
ALDOA
TPI
GAPDH
PGK1
PGAM1
ENO1
PKM1

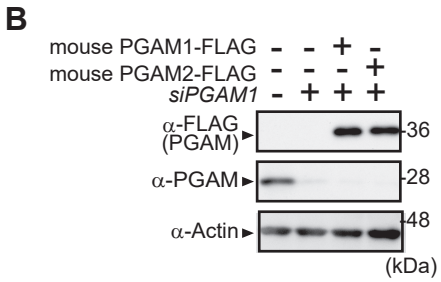
B
mouse PGAM1-FLAG
mouse PGAM2-FLAG
siPGAM1
α-FLAG (PGAM)
α-PGAM
α-Actin
36
28
48
(kDa)

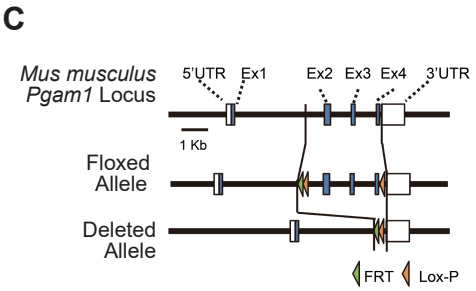
C
Mus musculus Pgam1 Locus
5'UTR
Ex1
Ex2
Ex3
Ex4
3'UTR
1 Kb
Floxed Allele
Deleted Allele
FRT
Lox-P

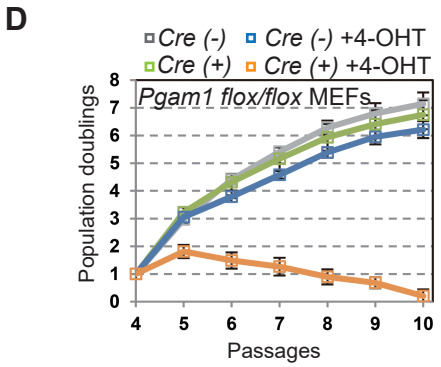
D
Cre (-)
Cre (-) +4-OHT
Cre (+)
Cre (+) +4-OHT
Pgam1 flox/flox MEFs
Population doublings
Passages

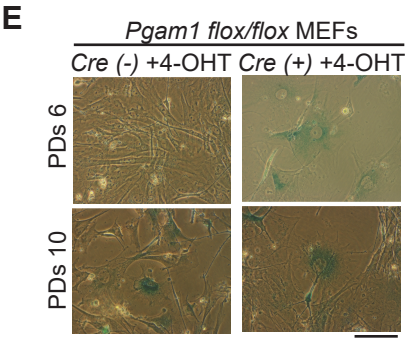
E
Pgam1 flox/flox MEFs
Cre (-) +4-OHT
Cre (+) +4-OHT
PDs 6
PDs 10

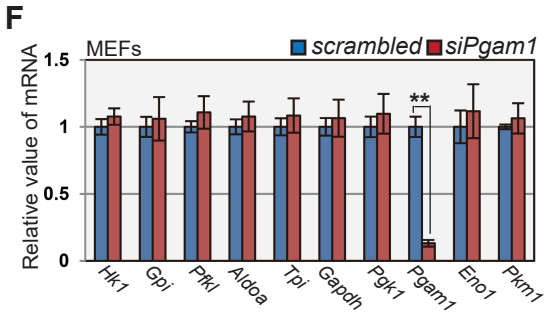
F
MEFs
scrambled
siPgam1
Relative value of mRNA
Hk1
Gpi
Pfkl
Aldoa
Tpi
Gapdh
Pgk1
Pgam1
Eno1
Pkm1

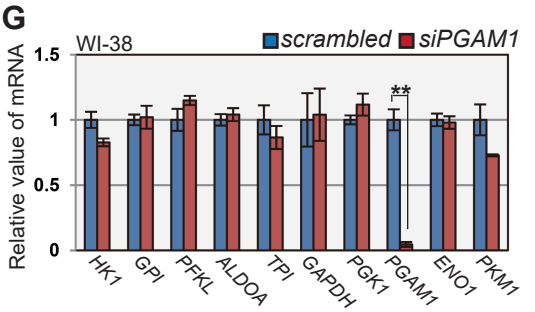
G
WI-38
scrambled
siPGAM1
Relative value of mRNA
HK1
GPI
PFKL
ALDOA
TPI
GAPDH
PGK1
PGAM1
ENO1
PKM1

Figure S4. Abrogation of PGAM in H1299 and standard cells.
Related to Figure 2

(A-B) H1299 cells with retroviral expression of empty vector, mouse PGAM1-FLAG, or mouse PGAM2-FLAG were prepared. Indicated cells were transfected with siRNA against endogenous human *PGAM1* or *scrambled* RNA. **(A)** The levels of glycolytic mRNAs were evaluated (n = 3). *P < 0.05 and **P < 0.005, Dunnett's multiple comparison test. **(B)** Immunoblotting detected both ectopically-expressed mouse PGAM-FLAG and endogenous human PGAM proteins in the indicated cells. **(C)** Construction of *Pgam1*-conditional KO mice is illustrated by a schematic diagram of the wild-type (WT), floxed, and *Pgam1* (exon 2–4) deleted alleles. **(D and E)** *Pgam1*$^{flox/flox}$ MEFs with or without *Cre-ER* were treated with 4-OHT, followed by serial passages according to the 3T3 cell culture protocol. *Cre (−)* and *(+)* indicate *Pgam1*$^{flox/flox}$ MEFs without or with *Cre-ER*, respectively. **(D)** Growth curves of indicated cells during 3T3 protocol. **(E)** SA-β-Gal staining was performed at passage 6 (PD6) and passage 10 (PD10) in *Pgam1* ablated MEFs (*Pgam1*$^{flox/flox}$ + *Cre-ER* with 4OHT) or control MEFs (*Pgam1*$^{flox/flox}$ with 4OHT). Scale bar indicates 200 μm. **(F and G)** Levels of glycolytic mRNAs in *siPgam1*-transfected standard cells. Primary MEFs **(F)** or human WI-38 **(G)** cells were prepared. Data are relative to expression in cells transfected with scrambled RNA. *P < 0.05 and **P < 0.005, Student's t-test. Data represent the mean ± SEM.

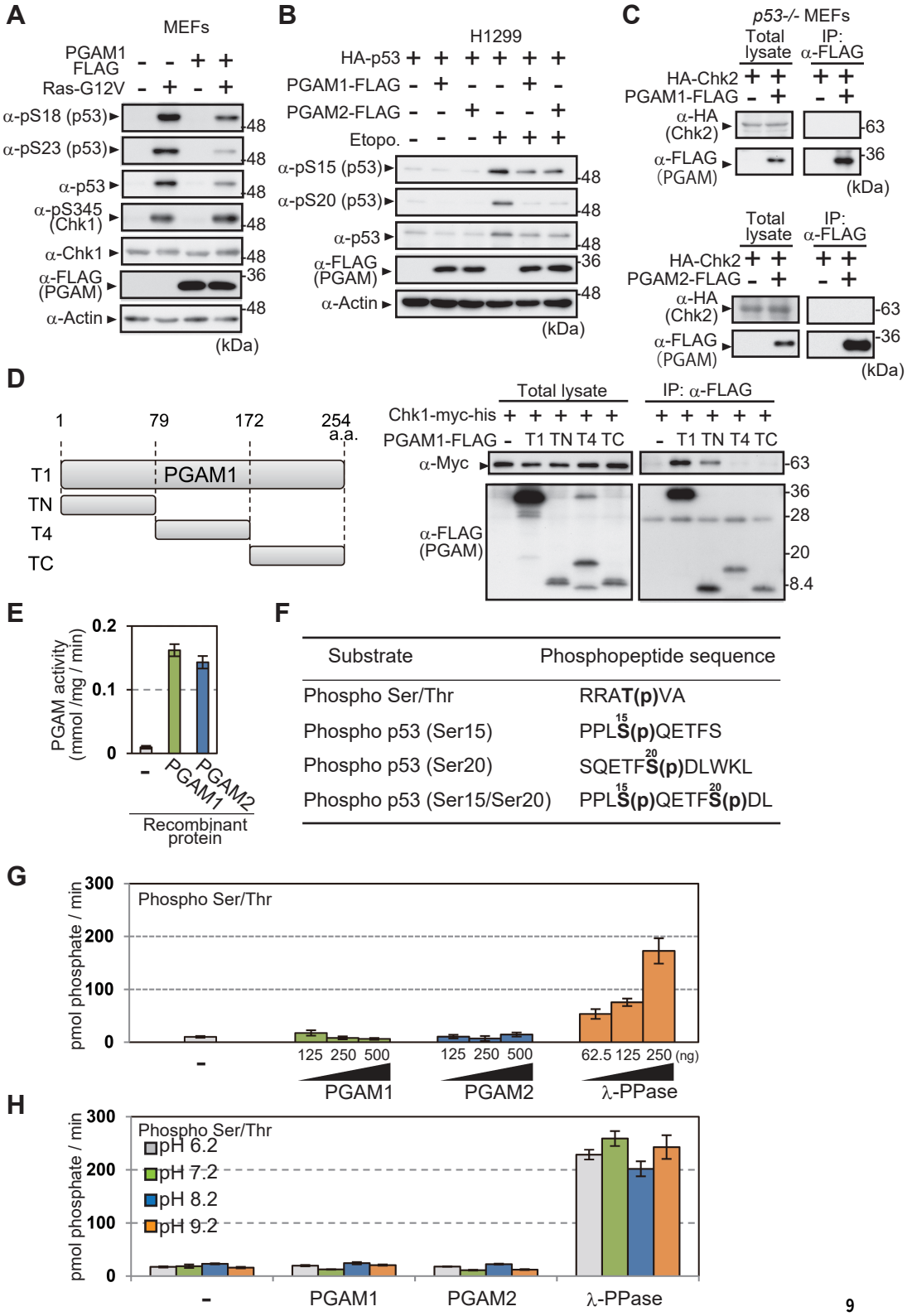
A
MEFs
PGAM1 FLAG - - + +
Ras-G12V - + - +
α-pS18 (p53)
α-pS23 (p53)
α-p53
α-pS345 (Chk1)
α-Chk1
α-FLAG (PGAM)
α-Actin
48
36
(kDa)
B
H1299
HA-p53 + + + + + +
PGAM1-FLAG - + - - + -
PGAM2-FLAG - - + - - +
Etopo. - - - + + +
α-pS15 (p53)
α-pS20 (p53)
α-p53
α-FLAG (PGAM)
α-Actin
48
36
(kDa)
C
p53-/- MEFs
Total lysate
IP: α-FLAG
HA-Chk2 + + + +
PGAM1-FLAG - + - +
α-HA (Chk2)
α-FLAG (PGAM)
63
36
(kDa)
Total lysate
IP: α-FLAG
HA-Chk2 + + + +
PGAM2-FLAG - + - +
α-HA (Chk2)
α-FLAG (PGAM)
63
36
(kDa)
D
1
79
172
254 a.a.
T1
TN
T4
TC
PGAM1
Total lysate
IP: α-FLAG
Chk1-myc-his + + + + + + + + + +
PGAM1-FLAG - T1 TN T4 TC - T1 TN T4 TC
α-Myc
α-FLAG (PGAM)
63
36
28
20
8.4
E
PGAM activity (mmol /mg / min)
0.2
0.1
0
-
PGAM1
PGAM2
Recombinant protein
F
Substrate | Phosphopeptide sequence
Phospho Ser/Thr | RRAT(p)VA
Phospho p53 (Ser15) | PPLS(p)QETFS
Phospho p53 (Ser20) | SQETFS(p)DLWKL
Phospho p53 (Ser15/Ser20) | PPLS(p)QETFS(p)DL
G
pmol phosphate / min
300
200
100
0
Phospho Ser/Thr
-
125 250 500
PGAM1
125 250 500
PGAM2
62.5 125 250 (ng)
λ-PPase
H
pmol phosphate / min
300
200
100
0
Phospho Ser/Thr
pH 6.2
pH 7.2
pH 8.2
pH 9.2
-
PGAM1
PGAM2
λ-PPase

Figure S5. The impact of PGAM on p53 phosphorylation and the assessment of protein phosphatase activity of PGAM. Related to Figure 3

(A-B) The impact of PGAM on the phosphorylation status of p53 was evaluated by western blotting. Primary MEFs were stressed by oncogenic Ras-G12V expression (A), while H1299 cells with indicated plasmids were treated with 100 μM Etoposide for 3 h (B). **(C)** The interaction between PGAM and Chk2 was examined in *p53*$^{-/-}$ MEFs transfected with HA-Chk2 and PGAM1- or 2-FLAG (upper and lower panels, respectively). **(D)** The evaluation of the interaction between Chk1 and various versions of PGAM1-FLAG. Left panel shows schematic diagram of various fragments of PGAM1. The binding of each fragment to Chk1 was assessed by co-immunoprecipitation (right panels). Extracts from *p53*$^{-/-}$ MEFs transfected with the indicated plasmids were immunoprecipitated with an anti-FLAG antibody. **(E)** Assessment of enzymatic activity for recombinant PGAM1 and PGAM2 protein. **(F)** The sequence of the phosphopeptides used for the *in vitro* phosphatase assay. RRAT(p)VA phosphopeptide (Phospho Ser/Thr) is compatible as a substrate for several serine/threonine phosphatases such as protein phosphatases 2A, 2B, and 2C. Phospho p53 (Ser15, Ser20, and Ser15/Ser20) phosphopeptides mimicked the p53 fragment phosphorylated at Ser15, Ser20, or Ser15/Ser20, respectively. **(G and H)** Phosphatase activity of recombinant PGAM1 and PGAM2 was evaluated. 5000 pmol phosphopeptides were incubated with recombinant PGAM1, PGAM2, or λPPase for 30 min, and the amount of released phosphate from phosphopeptides was monitored. **(G)** Phosphatase activity against phospho-Ser/Thr peptides was assessed with increasing amounts of recombinant PGAM (125, 250, and 500 ng) or λPPase (62.5, 125, and 250 ng). **(H)** Phosphatase activity against phospho-Ser/Thr peptides was assessed using 500 ng PGAM1 or PGAM2, or 250 ng λPPase in the indicated pH conditions. Data represent the mean ± SEM.

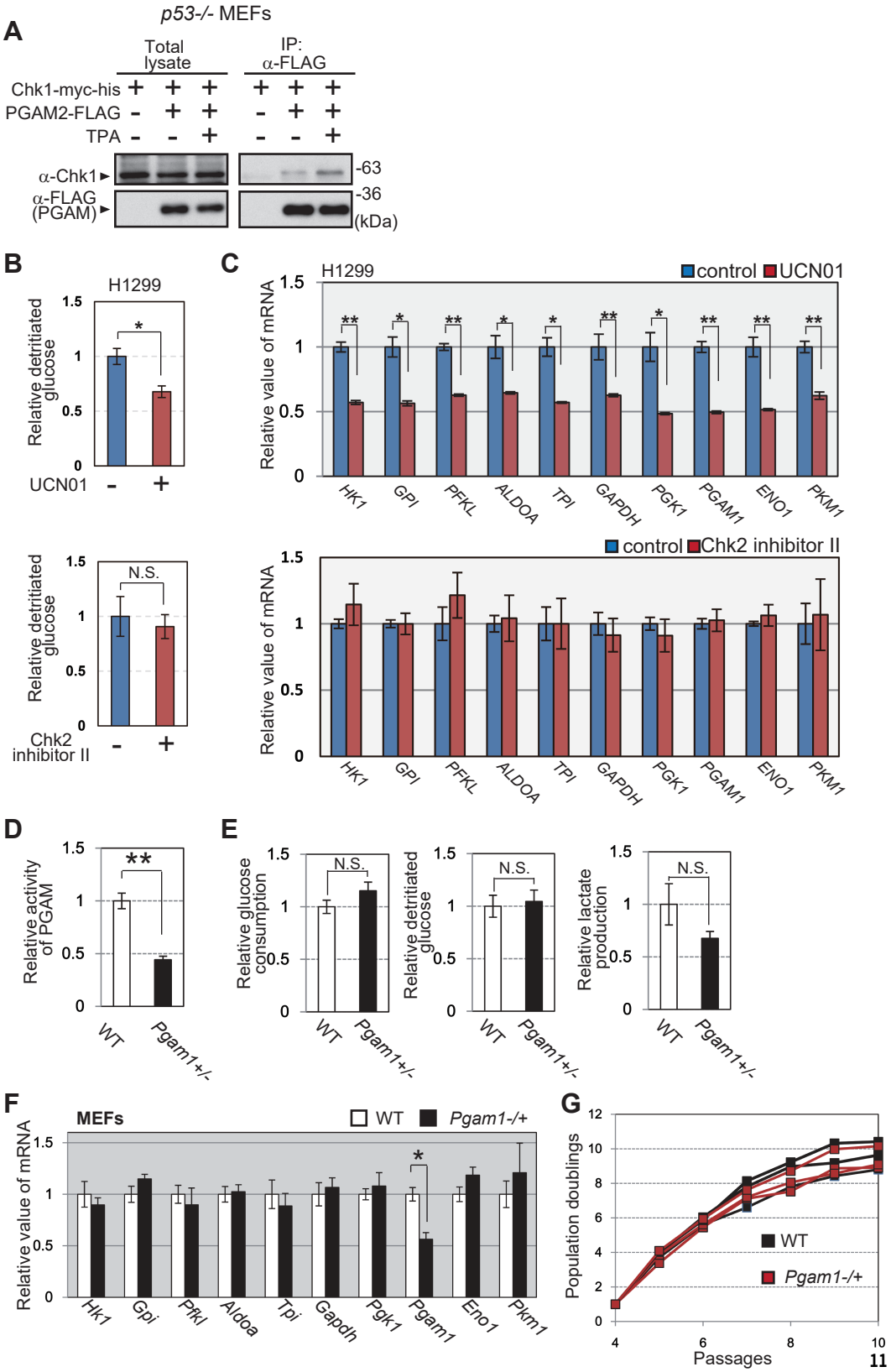
A
p53-/- MEFs
Total lysate
IP: α-FLAG
Chk1-myc-his + + + + + +
PGAM2-FLAG - + + - + +
TPA - - + - - +
α-Chk1
α-FLAG (PGAM)
-63
-36
(kDa)
B
H1299
Relative detritiated glucose
UCN01 - +
N.S.
Chk2 inhibitor II - +
C
H1299
control UCN01
Relative value of mRNA
HK1 GPI PFKL ALDOA TPI GAPDH PGK1 PGAM1 ENO1 PKM1
control Chk2 inhibitor II
D
Relative activity of PGAM
WT Pgam1+/-
E
Relative glucose consumption
Relative detritiated glucose
Relative lactate production
N.S.
F
MEFs
WT Pgam1-/+
Relative value of mRNA
Hk1 Gpi Pfkl Aldoa Tpi Gapdh Pgk1 Pgam1 Eno1 Pkm1
G
Population doublings
Passages
WT
Pgam1-/+

Figure S6. Impact of Chk1 on glycolytic mRNAs. Related to Figure 4

(A) The impact of TPA treatment on the interaction between PGAM and Chk1. $p53^{-/-}$ MEFs with expression of Chk1-myc-his and PGAM2-FLAG were treated with or without 0.1 μg/ml TPA for 48 hours, followed by treatment with MG132 for 3 h. The cell lysates were immunoprecipitated with an anti-FLAG antibody. **(B and C)** Effect of UCN01 (Chk1 inhibitor) or Chk2-inhibitor II on glycolytic profiles in H1299 cells (*n* = 3). H1299 were exposed to 500 nM UCN01 or 10 μM Chk2 inhibitor II for 12 h (upper and lower panel, respectively). **(B)** Glycolytic flux was evaluated in indicated cells (n=3). **(C)** The glycolytic mRNA expression was detected by qRT-PCR. Data are relative to expression in control cells. **P* < 0.05 and ***P* < 0.005, Student's t-test. **(D-G)** Cytological characterization of *Pgam1* heterozygous KO MEFs. **(D)** Measurement of total PGAM enzymatic activity in WT (*n* = 3) and $Pgam1^{+/-}$ MEFs (*n* = 3). **(E)** Glucose consumption (left), glucose flux (middle), and lactate production (right) in WT (*n* = 3) or $Pgam1^{+/-}$ MEFs (*n* = 3). **(F)** Comparison of glycolytic mRNAs by real-time qRT-PCR between wild-type (WT) (*n* = 3) and $Pgam1^{+/-}$ MEFs (*n* = 3). Data are shown as relative values against those in WT. **(G)** Growth curves of WT and $Pgam1^{+/-}$ MEFs Three independent lines of each MEF were passaged according to 3T3 cell culture protocol. **P* < 0.05 and ***P* < 0.005, Student's t-test. Data represent the mean ± SEM.

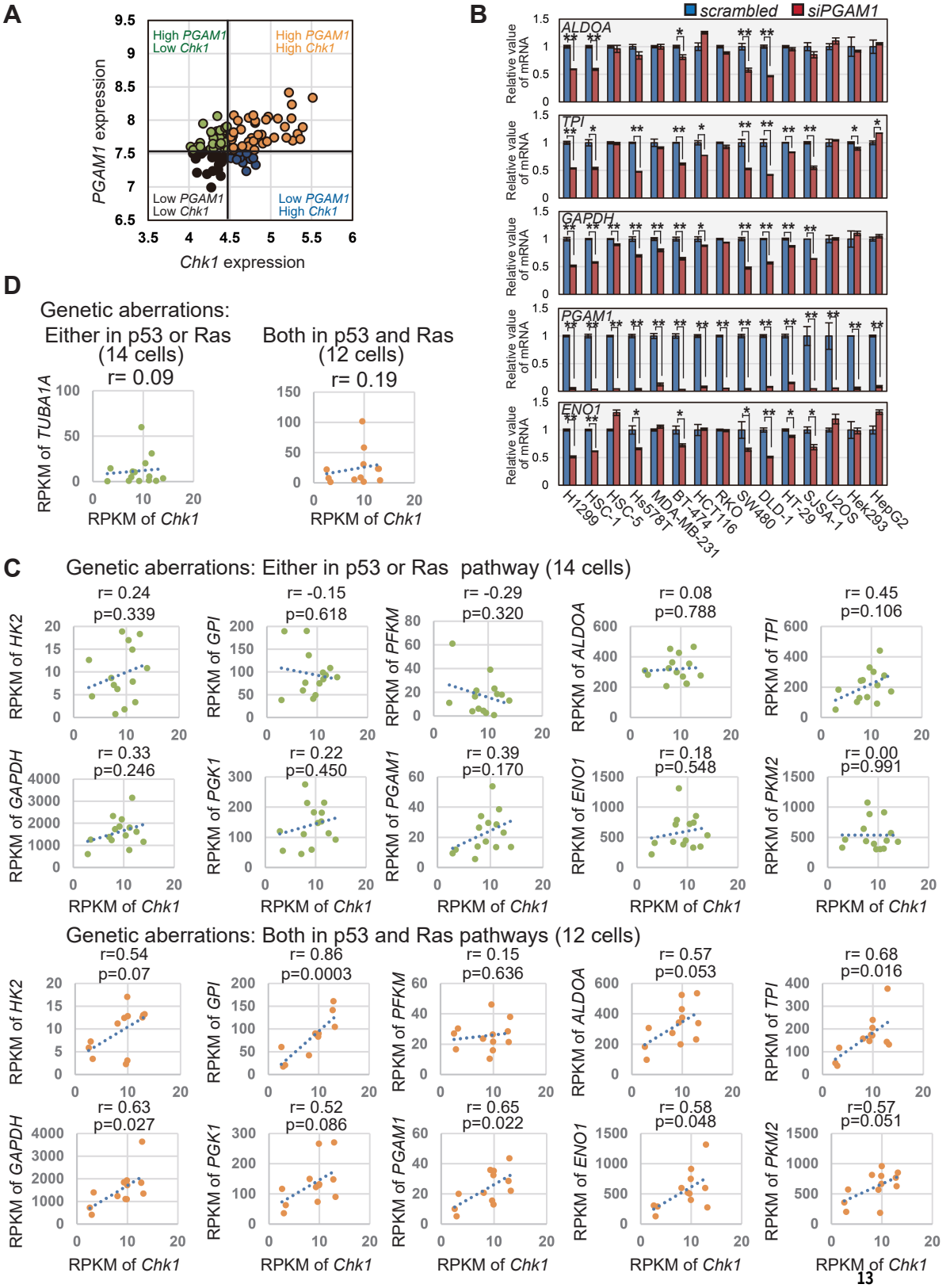
A
High PGAM1
Low Chk1
High PGAM1
High Chk1
Low PGAM1
Low Chk1
Low PGAM1
High Chk1
PGAM1 expression
Chk1 expression
B
scrambled
siPGAM1
ALDOA
TPI
GAPDH
PGAM1
ENO1
Relative value of mRNA
H1299
HSC-1
HSC-5
Hs578T
MDA-MB-231
BT-474
HCT116
RKO
SW480
DLD-1
HT-29
SUSA-1
U2OS
Hek293
HepG2
D
Genetic aberrations:
Either in p53 or Ras (14 cells)
r= 0.09
Both in p53 and Ras (12 cells)
r= 0.19
RPKM of TUBA1A
RPKM of Chk1
C
Genetic aberrations: Either in p53 or Ras pathway (14 cells)
r= 0.24
p=0.339
r= -0.15
p=0.618
r= -0.29
p=0.320
r= 0.08
p=0.788
r= 0.45
p=0.106
RPKM of HK2
RPKM of GPI
RPKM of PFKM
RPKM of ALDOA
RPKM of TPI
r= 0.33
p=0.246
r= 0.22
p=0.450
r= 0.39
p=0.170
r= 0.18
p=0.548
r= 0.00
p=0.991
RPKM of GAPDH
RPKM of PGK1
RPKM of PGAM1
RPKM of ENO1
RPKM of PKM2
RPKM of Chk1
Genetic aberrations: Both in p53 and Ras pathways (12 cells)
r=0.54
p=0.07
r= 0.86
p=0.0003
r= 0.15
p=0.636
r= 0.57
p=0.053
r= 0.68
p=0.016
r= 0.63
p=0.027
r= 0.52
p=0.086
r= 0.65
p=0.022
r= 0.58
p=0.048
r=0.57
p=0.051

Figure S7. Analysis of patient prognosis and cell lines for lung cancer. Related to Figure 5

(A) The comparison plot for *PGAM1* and *Chk1* levels in 104 NSCLC patients (Dataset Jacob-00182-MSK). According to the expression levels of *PGAM1* or *Chk1*, NSCLC patients were categorized into four groups, as shown in Figure 5A. Cut-off points for *PGAM1* and *Chk1* were 7.546 and 4.509, respectively. **(B)** The levels of the glycolytic mRNAs, *ALDO1, TPI, GAPDH* and *ENO1*, were evaluated in *PGAM1*-knockdown cancer cell lines (n = 3 per cell line). Values for indicated targets are relative to those in cells transfected with scrambled siRNA. *P < 0.05 and **P < 0.005, Student's t-test. **(C and D)** Association of expression levels among indicated genes was evaluated in dataset of 26 non-small cell lung adenocarcinoma cell lines as shown in Figure 5C. **(C)** Association between *Chk1* and glycolytic enzymes in two indicated subgroups; 14 cells with genetic aberration either in p53 or Ras pathway, and 12 cells mutated in both. **(D)** Association between expressions of *Chk1* and *TUBA1A*. Correlation-coefficient and significance-probability were presented as r-value and p-value, respectively.

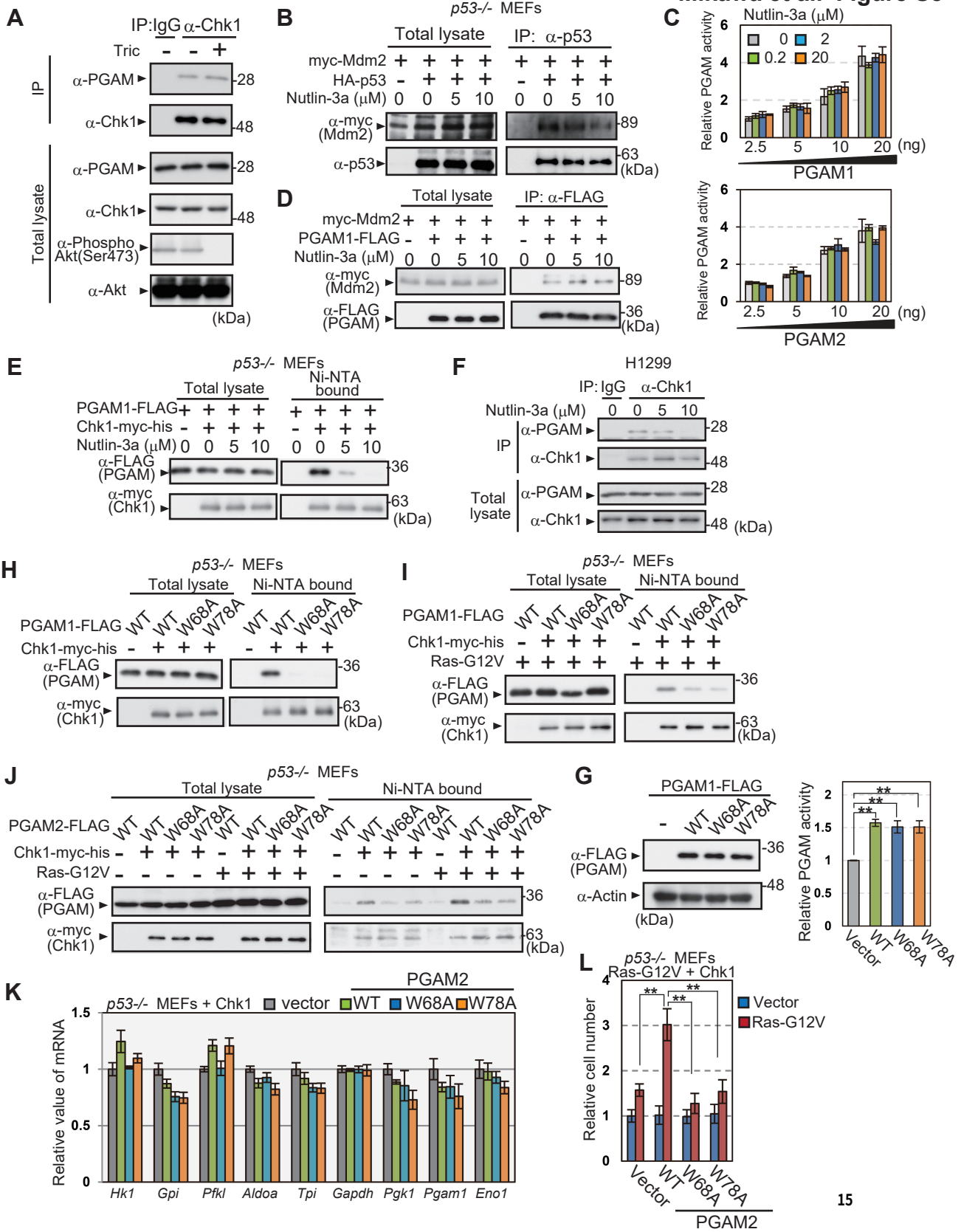
A
IP:IgG α-Chk1
Tric - - +
IP
α-PGAM
28
α-Chk1
48
Total lysate
α-PGAM
28
α-Chk1
48
α-Phospho Akt(Ser473)
α-Akt
(kDa)
B
p53-/- MEFs
Total lysate
IP: α-p53
myc-Mdm2 + + + + + + + +
HA-p53 - + + + - + + +
Nutlin-3a (μM) 0 0 5 10 0 0 5 10
α-myc (Mdm2)
89
α-p53
63
(kDa)
C
Nutlin-3a (μM)
0 2 0.2 20
Relative PGAM activity
2.5 5 10 20 (ng)
PGAM1
PGAM2
D
Total lysate
IP: α-FLAG
myc-Mdm2 + + + + + + + +
PGAM1-FLAG - + + + - + + +
Nutlin-3a (μM) 0 0 5 10 0 0 5 10
α-myc (Mdm2)
89
α-FLAG (PGAM)
36
(kDa)
E
p53-/- MEFs
Total lysate
Ni-NTA bound
PGAM1-FLAG + + + + + + + +
Chk1-myc-his - + + + - + + +
Nutlin-3a (μM) 0 0 5 10 0 0 5 10
α-FLAG (PGAM)
36
α-myc (Chk1)
63
(kDa)
F
H1299
IP: IgG α-Chk1
Nutlin-3a (μM) 0 0 5 10
IP
α-PGAM
28
α-Chk1
48
Total lysate
α-PGAM
28
α-Chk1
48 (kDa)
H
p53-/- MEFs
Total lysate
Ni-NTA bound
PGAM1-FLAG WT WT W68A W78A WT WT W68A W78A
Chk1-myc-his - + + + - + + +
α-FLAG (PGAM)
36
α-myc (Chk1)
63
(kDa)
I
p53-/- MEFs
Total lysate
Ni-NTA bound
PGAM1-FLAG WT WT W68A W78A WT WT W68A W78A
Chk1-myc-his - + + + - + + +
Ras-G12V + + + + + + + +
α-FLAG (PGAM)
36
α-myc (Chk1)
63
(kDa)
J
p53-/- MEFs
Total lysate
Ni-NTA bound
PGAM2-FLAG WT WT W68A W78A WT WT W68A W78A WT WT W68A W78A WT WT W68A W78A
Chk1-myc-his - + + + - + + + - + + + - + + +
Ras-G12V - - - - + + + + - - - - + + + +
α-FLAG (PGAM)
36
α-myc (Chk1)
63
(kDa)
G
PGAM1-FLAG
- WT W68A W78A
α-FLAG (PGAM)
36
α-Actin
48
(kDa)
Relative PGAM activity
Vector WT W68A W78A
K
PGAM2
p53-/- MEFs + Chk1 vector WT W68A W78A
Relative value of mRNA
Hk1 Gpi Pfkl Aldoa Tpi Gapdh Pgk1 Pgam1 Eno1
L
p53-/- MEFs
Ras-G12V + Chk1
Vector
Ras-G12V
Relative cell number
Vector WT W68A W78A
PGAM2

Figure S8. Nutlin and binding-deficient mutations in PGAM interfere with the interaction between PGAM and Chk1, but not with PGAM enzymatic activity. Related to Figure 5, 6 and 7

(A) The impact of AKT inhibition against PGAM-Chk1 interaction. H1299 cells were treated with Triciribine. Immunoprecipitation assay were performed using anti-Chk1 antibody. Ser473 phosphorylation on AKT was evaluated. **(B)** The interaction between p53 and Mdm2 during Nutlin-3a treatment was evaluated by immunoprecipitation assay. *p53*$^{-/-}$ MEFs expressing the indicated vectors were exposed to 5 μM or 10 μM Nutlin-3a for 48 h, followed by treatment with 20 μM MG132 for 3 h. The lysates were immunoprecipitated with anti-p53 antibody. **(C)** Enzymatic activity of recombinant PGAM1 and 2 proteins was assessed in the presence of Nutlin-3a. Various amounts of recombinant PGAM1 and 2 proteins (2.5, 5, 10, and 20 ng) were incubated with indicated concentrations of Nutlin-3a (upper and lower panel, respectively). Data represent the mean ± SEM. **(D)** The effect of Nutlin-3a on PGAM1 and Mdm2 interaction was evaluated by the immunoprecipitation assay. **(E)** The evaluation of PGAM1 and Chk1 interaction under Nutlin-3a treatment by the immunoprecipitation assay. **(F)** The effect of Nutlin-3a on endogenous PGAM-Chk1 binding in H1299 cells. Cells were exposed to Nutlin-3a for 48 h. After treatment with 20 μM MG132 for 3 h, the immunoprecipitation assay was performed, using the indicated antibodies. **(G)** PGAM enzymatic activity in Chk1-expressing *p53*$^{-/-}$ MEFs retrovirally infected with the indicated vectors (empty vector, PGAM1-WT-FLAG, PGAM1-W68A-FLAG, and PGAM1-W78A-FLAG) (*n* = 3 each; right panel). Protein levels for various versions of PGAM1-FLAG were shown by western blotting (left panels). **(H and I)** His-tagged protein pulldown assay. The Chk1-binding activity of PGAM1 mutants (W68A and W78A) compared to that of PGAM1-WT was analyzed in the absence or presence of oncogenic Ras (H and I, respectively). **(J)** The interaction of PGAM2-W68A or -W78A mutant with Chk1. The Chk1-binding activity in various versions of PGAM2 (WT, W68A, or W78A) was assessed by His-tagged protein pulldown assay in the presence or absence of Ras-G12V. Chk1-expressing *p53*$^{-/-}$ MEFs with indicated genes were analyzed. **(K)** Comparison of mRNA levels for glycolytic enzymes in indicated Chk1-expressing *p53*$^{-/-}$ MEFs with PGAM2 variants (WT, W68A, or W78A) (*n* = 3). The data are relative to expression in control cells with the empty vector. **(L)** Comparison of cell proliferation *in vitro*. The effect of PGAM2 variants (WT, W68A, or W78A) on cell growth was assessed by crystal violet staining in Chk1-expressing

p53$^{-/-}$ MEFs with or without Ras-G12V as shown in Figure 7F. The staining intensities for three independent assays were shown as relative cell numbers against control. **$P < 0.005$, Dunnett's multiple comparison test. Data represent the mean ± SEM.

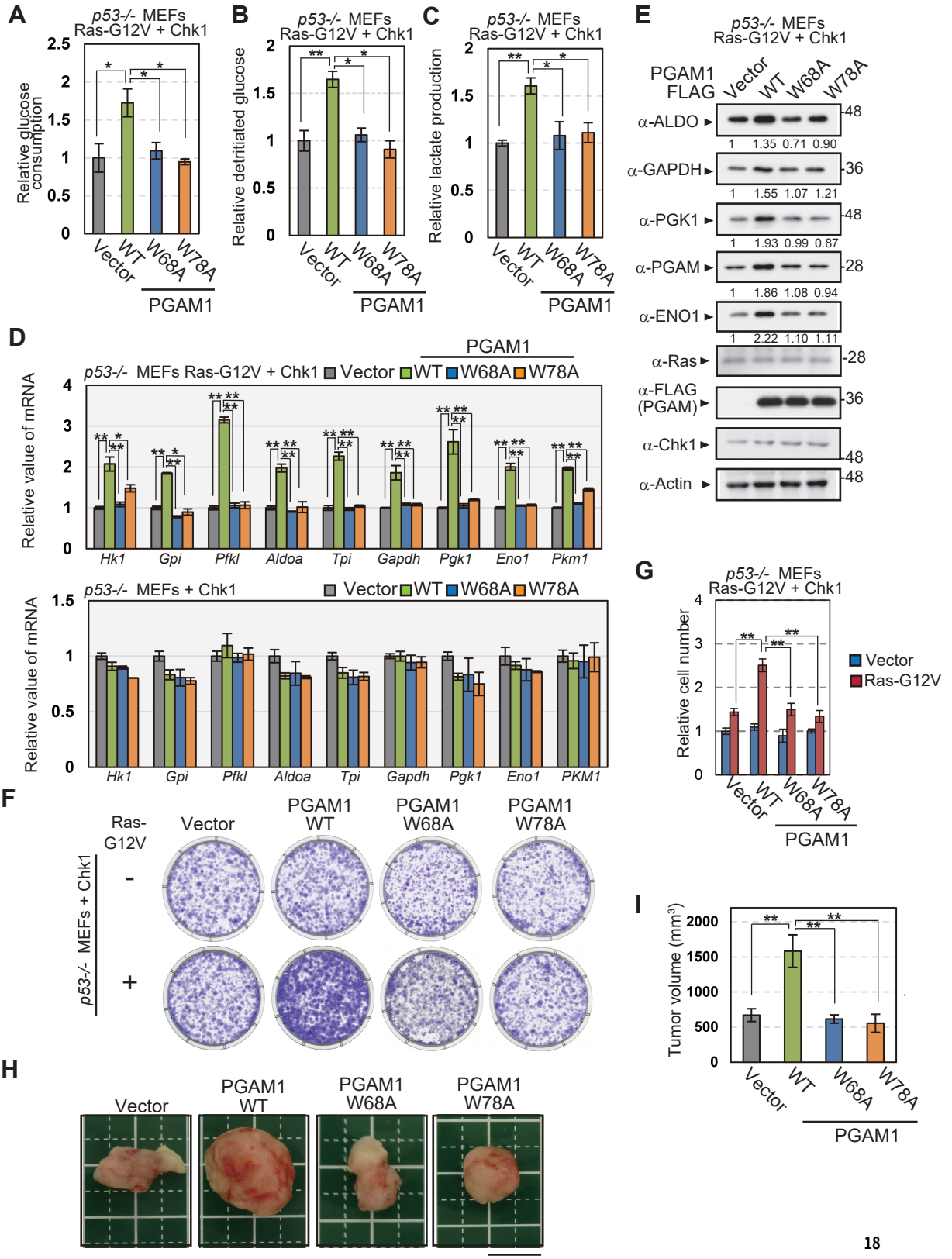
A
p53-/- MEFs
Ras-G12V + Chk1
Relative glucose consumption
Vector
WT
W68A
W78A
PGAM1
B
Relative detriated glucose
C
Relative lactate production
D
Relative value of mRNA
Hk1
Gpi
Pfkl
Aldoa
Tpi
Gapdh
Pgk1
Eno1
Pkm1
p53-/- MEFs + Chk1
PKM1
E
PGAM1 FLAG
α-ALDO
α-GAPDH
α-PGK1
α-PGAM
α-ENO1
α-Ras
α-FLAG (PGAM)
α-Chk1
α-Actin
1 1.35 0.71 0.90
1 1.55 1.07 1.21
1 1.93 0.99 0.87
1 1.86 1.08 0.94
1 2.22 1.10 1.11
G
Relative cell number
Vector
Ras-G12V
F
Ras-G12V
PGAM1 WT
PGAM1 W68A
PGAM1 W78A
H
I
Tumor volume (mm3)

Figure S9. PGAM1 mutants with W68A or W78A abolished the enhancement of glycolysis and proliferation in oncogenic Ras expressing cells. Related to Figure 7

(A-E) Comparison of glycolytic profiles among the cells expressing PGAM1 variants (WT, W68A, or W78A) in the presence of Ras-G12V. Glucose consumption **(A)**, glucose flux **(B)**, and lactate production **(C)** were analyzed among indicated cells on the common genetic background of *p53*$^{-/-}$ with Ras-G12V and Chk1 (n = 3). The mRNA and protein levels of glycolytic enzymes were also evaluated in indicated cells **(D and E)**. **(F and G)** The effect of indicated PGAM1 variants on cell growth *in vitro*. Crystal-violet staining was assessed in Chk1-expressing *p53*$^{-/-}$ MEFs with or without Ras-G12V **(F)**. Intensities of crystal-violet staining were measured **(G)**. **(H and I)** *in vivo* tumor growth assay in nude mice. *p53*$^{-/-}$ MEFs, expressing Ras-G12V, Chk1, and the indicated versions of PGAM1, were injected subcutaneously into nude mice (n=6). **(H)** Representative images of tumors. **(I)** Measurement of tumor volumes are shown. **P* < 0.05 and **P < 0.005, Dunnett's multiple comparison test. Data represent the mean ± SEM.

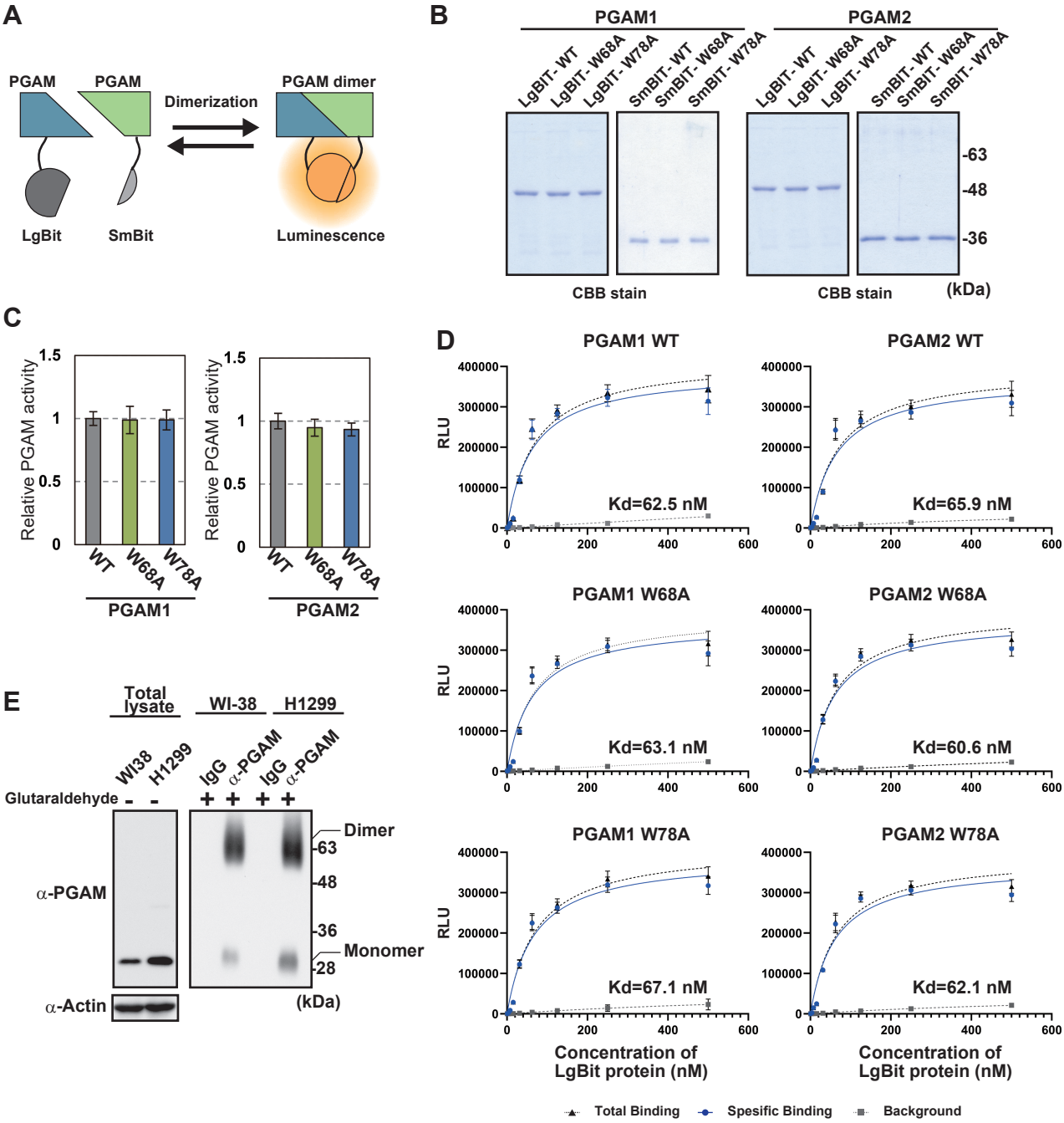
A
PGAM
PGAM
Dimerization
PGAM dimer
LgBit
SmBit
Luminescence
B
PGAM1
PGAM2
LgBIT- WT
LgBIT- W68A
LgBIT- W78A
SmBIT- WT
SmBIT- W68A
SmBIT- W78A
-63
-48
-36
CBB stain
CBB stain
(kDa)
C
Relative PGAM activity
1.5
1
0.5
0
WT
W68A
W78A
PGAM1
PGAM2
D
PGAM1 WT
PGAM2 WT
PGAM1 W68A
PGAM2 W68A
PGAM1 W78A
PGAM2 W78A
RLU
Kd=62.5 nM
Kd=65.9 nM
Kd=63.1 nM
Kd=60.6 nM
Kd=67.1 nM
Kd=62.1 nM
Concentration of LgBit protein (nM)
Total Binding
Spesific Binding
Background
E
Total lysate
WI-38
H1299
WI38
H1299
IgG
α-PGAM
Glutaraldehyde
α-PGAM
α-Actin
Dimer
Monomer
(kDa)

Figure S10. The dimerization efficiency in various versions of PGAM1 and PGAM2. Related to Figure 7

(A) Schematic diagrams of NanoBiT systems. Dimerization of PGAM proteins with large and small NanoBiT tag produces luminescence. **(B)** Coomassie Brilliant Blue staining for indicated recombinant proteins prepared from bacteria. **(C)** Measurement of PGAM enzymatic activity in indicated LgBiT-tagged PGAM recombinant proteins. **(D)** Saturated binding of SmBiT-PGAM to LgBiT-PGAM was assessed. 0.25 nM SmBiT-PGAM proteins were incubated with various concentration of indicated LgBiT-PGAM proteins. NanoBiT luminescence of dimerized PGAM proteins was measured. The left panels show dimerization of PGAM1 WT (top), PGAM1 W68A (middle), PGAM1 W78A (bottom), while the right panels indicate those of PGAM2 WT (top), PGAM2 W68A (middle) and PGAM2 W78A (bottom). Triangle; total binding curve of the complex between LgBiT and SmBit proteins. Square; background curve of LgBiT proteins only. Specific binding curve (circle) is obtained by subtracting background signals from total binding ones. Binding dissociation constant (Kd) was estimated from the curve of specific binding. **(E)** Evaluation of monomer and dimer forms of PGAM in H1299 and WI-38 cells. After 100kd cutoff filtration, the protein extracts from indicated cells were immunoprecipitated by anti-PGAM1 antibody. After the elution of PGAM protein from PGAM1 antibody-conjugated beads by specific peptides, eluted proteins were cross-linked by 0.5% glutaraldehyde for 5 min. Immunoblotting detected monomer or dimer of PGAM proteins (right panel). Left panels showed the immunoblotting in total cell lysates of indicated cells without cross-link.

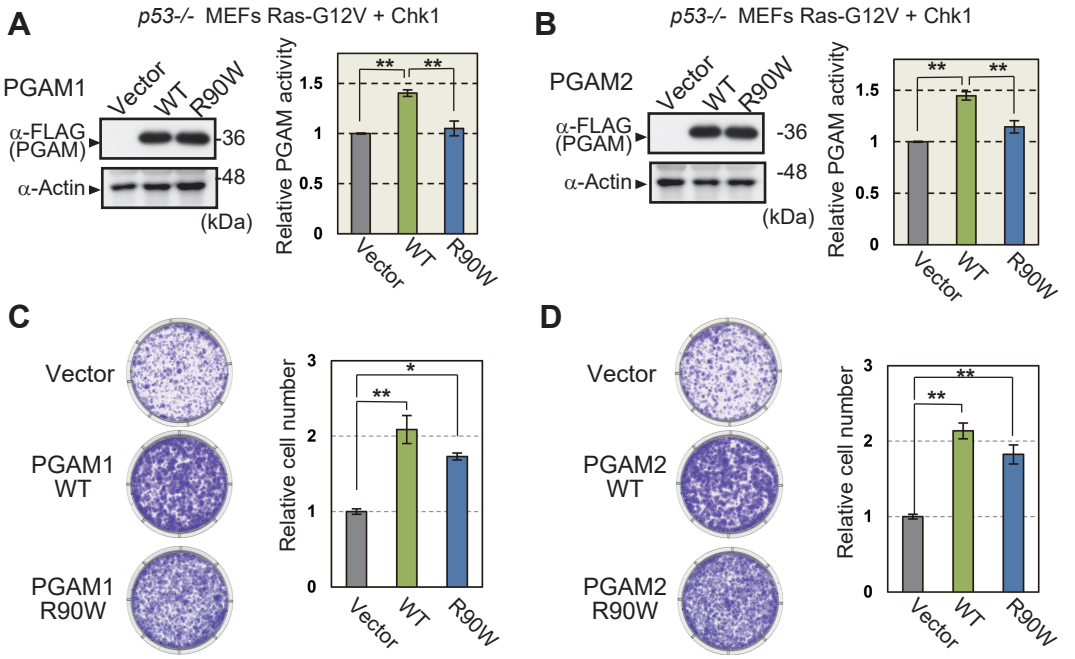
A
p53-/- MEFs Ras-G12V + Chk1
PGAM1
Vector
WT
R90W
α-FLAG (PGAM)
α-Actin
-36
-48
(kDa)
Relative PGAM activity
1.5
1
0.5
0
**
**
Vector
WT
R90W
B
p53-/- MEFs Ras-G12V + Chk1
PGAM2
Vector
WT
R90W
α-FLAG (PGAM)
α-Actin
-36
-48
(kDa)
Relative PGAM activity
1.5
1
0.5
0
**
**
Vector
WT
R90W
C
Vector
PGAM1 WT
PGAM1 R90W
Relative cell number
3
2
1
0
*
**
Vector
WT
R90W
D
Vector
PGAM2 WT
PGAM2 R90W
Relative cell number
3
2
1
0
**
**
Vector
WT
R90W

Figure S11. The impact of enzymatic mutant PGAM-R90W on cell growth. Related to Figure 7

(A and B) Enzymatic mutation *R90W* was introduced in PGAM1 (A) and PGAM2 (B). Western blotting was performed to detect FLAG tagged PGAM proteins (left panels). PGAM enzymatic activities were measured in indicated cells (right panels). **(C and D)** Crystal-violet (CV) staining was assessed in indicated cells to evaluate their proliferative capacity (left panels). The intensities of CV staining were evaluated (right panels).

Table S1. The list of cancer-related genetic aberrations

	H1299	HSC-1	HSC-5	Hs578T	MDA-MB-231	BT-474	HCT116	RKO	SW480	DLD-1	HT-29	SJSA-1	U2OS	Hek293	HepG2
ABL1		*[1]	*[1]	*K7R*			*Y257C*	*F747I*						*[1]	
AKT1		*[1]	*[1]											*[1]	
ALK		*[1]	*[1]											*[1]	
APC		*[1]	*[1]					*K1454E*	*Q1338**	*I1417fs*2 K993N R727M*	*E853* T1556fs**			*[1]	
ATM		*[1]	*[1]		*N1005I*	*E2468K*	*A1127V*		*R2461P*					*[1]	*V2906I*
BRAF		*[1]	*[1]		*G464V*			*V600E*			*V600E T119S*			*[1]	
CDH1		*[1]	*[1]				*H121fs*94*							*[1]	
CDKN2A		*[1]		*c.1_471 de*	*c.1_471 de*		*R24fs*20 E74fs*15*							*[1]	
CSF1R		*[1]	*[1]											*[1]	
CTNNB1		*[1]	*[1]				*S45del*							*[1]	*W25_I140de*
EGFR		*amp*[2]			*L469W*									*[1]	
ERBB2		*[1]	*[1]					*L796P*						*[1]	
ERBB4		*[1]	*[1]											*[1]	
EZH2		*[1]	*[1]					*E169K*		*R418Q*				*[1]	
FBXW7		*[1]	*[1]											*[1]	
FGFR1		*[1]	*[1]				*A343V*	*P150L*		*A268S*				*[1]	
FGFR2		*[1]	*[1]				*P582L*							*[1]	
FGFR3		*[1]	*[1]											*[1]	
FLT3		*[1]	*[1]				*V197A P986fs*>8*							*[1]	
GNA11		*[1]	*[1]											*[1]	
GNAS		*[1]	*[1]				*Y316C*			*K338N*				*[1]	
GNAQ		*[1]	*[1]				*A102G*							*[1]	
HNF1A		*[1]	*[1]	*K273E*		*Q495**	*P174fs*51*	*P379fs*5*						*[1]	
HRAS		*[1]	*[1]	*G12D*										*[1]	
IDH1		*[1]	*[1]				*S261L*			*G97D*				*[1]	

Table S1. The list of cancer-related genetic aberrations (continued)

	H1299	HSC-1	HSC-5	Hs578T	MDA-MB-231	BT-474	HCT116	RKO	SW480	DLD-1	HT-29	SJSA-1	U2OS	Hek293	HepG2
IDH2		*1	*1					*G190D*						*1	
JAK2		*1	*1											*1	
JAK3		*1	*1											*1	
KDR		*1	*1											*1	
KIT		*1	*1							*R135H*				*1	
KRAS		*1	*1		*G13D*		*G13D*		*G12V*	*G13D*		*Q61H*		*1	
MET		*1	*1				*L238fs*25*							*1	
MLH1		*1	*1				*S252**	*L323M*		*A120S*				*1	
MPL		*1	*1											*1	
NOTCH1		*1	*1				*P915L G1195R*	*Q2343R*						*1	
NPM1		*1	*1											*1	
NRAS	*Q61K*	*1	*1									*Q61K*		*1	*Q61L*
PDGFRA		*1	*1		*Y172F*									*1	
PIK3CA		*1				*K111N*	*H1047R*	*H1047R*		*D549N E545K*	*P449T*			*1	
PTEN		*1												*1	
PTPN11		*1	*1											*1	
RB1		*1	*1											*1	
RET		*1	*1											*1	
SMAD4		*1	*1								*Q311**			*1	
SMARCB1		*1	*1											*1	
SMO		*1	*1				*V404M*			*T640A*				*1	
SRC		*1	*1											*1	
STK11		*1	*1											*1	
TP53	*del*	*V173L*	*1	*V157F*	*R280K*	*E285K*			*P309S R273H*	*S241F*	*R273H*	*Mdm2 amp*2*		*1	
VHL		*1	*1												

Table S1. List of cancer-related mutations in 15 cancer cell lines. Related to Figure 5

Summary of identified mutations in 15 cancer cell lines. These cells were tested in Figure 5B and S7B. Fifty cancer-related genes were proposed by Tsongalis et al (Tsongalis et al., 2014).

Gene mutations in 15 cancer cells were described in the following literatures (Cancer Genome Atlas Research, 2008; Fujii et al., 1995; Hori et al., 2009; Klijn et al., 2015; Oliner et al., 1992).

*[1] Not determined,

*[2] amp stands for amplification,

Table S2 Genetic aberrations of lung adenocarcinoma cell lines

Cells having genetic aberrations either in p53 or Ras pathway

	Genetic aberrations				
	EGFR	***KRAS***	***NRAS***	***HRAS***	***p53***
A427		*G12D*			
A549		*G12S*			
H1437					*R267P*
H1648					*L35Fs*8*
H1703					*c919+1G>T*
H1819					*c933+1G>T*
H2126					*E62**
H2228					*Q331**
H2347		*L19F* *R481H*	*Q61R*		
H322					*Arg248Leu*
PC-3					*K139fs*31*
RERF-LC-KJ					*E224D*
VMRC-LCD					*R175H*
LC2					*S241C*

Table S2. Genetic aberrations of lung adenocarcinoma cell lines (continued)

Cells having genetic aberrations both in p53 and Ras pathways

	Genetic aberrations				
	EGFR	***KRAS***	***NRAS***	***HRAS***	***p53***
ABC-1	*L858R*				*P278S*
H1299			*Q61K*		*c1_954>AAG*
H1650	*E746_A750del*				*c673-2A>G*
H1975	*T790M, L858R*				*R273H*
II-18	*L858R*				*K164**
PC-14	*E746_A750del*				*Arg248Trp*
PC-7	*G719S*	*G12V*			*His214Arg*
PC-9	*E746_A750del L858R*				*Arg248Gln*
RERF-LC-MS		*K12S*			*F134fs*14*
RERF-LC-OK	*L858R*				*F113C*
RERF-LC-ad1		*G12A*			*P278F*
RERF-LC-ad2	*L747_A750>P*				*A159V*

Table S2. Classification of 26 non-small cell lung cancer (NSCLC) cell lines. Related to Figure 5

26 NSCLC cell lines were classified into two subgroups according to gene aberrations of *p53* and *Ras* pathways.

Upper list shows 14 cells harboring genetic aberrations either in p53 or Ras pathway, while lower list indicates 12 cells with genetic aberrations in both pathways.

Gene mutations of NSCLC cells were described in the following literatures (Barretina et al., 2012; Chen et al., 1993; Fujita et al., 1999; Iwakawa et al., 2010; Kashii et al., 1994; Kaufman et al., 2017; Nagai et al., 2005; Notsuda et al., 2013; Wei et al., 2003)

Table S3. The primer sequences for real-time qRT-PCR

Name	Sequence
mouse *Rpl13a* qRT Fw	5’- TGC TGC TCT CAA GGT TGT TCG -3’
mouse *Rpl13a* qRT Re	5’- GCC TTT TCC TTC CGT TTC TCC -3’
mouse *Hk1* qRT Fw	5'-AAG AAT GGC CTC TCC CGG-3
mouse *Hk1* qRT Re	5'-CGC CGA GAT CCA GTG CAA TG-3'
mouse *Hk2* qRT Fw	5'-ATA TGG TTG CCT CAT CTT GG-3'
mouse *Hk2* qRT Re	5'-CTC CCT CCC TCC CAA TG-3'
mouse *Hk3* qRT Fw	5'-ATT CCT GGA TGC ATA CCC CGT -3'
mouse *Hk3* qRT Re	5'-GCC GCT GCA CCT AAA ACC TTT -3'
mouse *Gpi* qRT Fw	5'-CCA ATG CAG AGA CAG CAA AGG-3'
mouse *Gpi* qRT Re	5'-CACTTTGGCCGTGTTCGTAGA-3'
mouse *Pfkm* qRT Fw	5'-TGG AGC GAC TTG CTG AAT GAT -3'
mouse *Pfkm* qRT Re	5'-TCA TTG TCG ATT GAG CCA ACC -3'
mouse *Pfkl* qRT Fw	5'-GCT GCA ATG GAG TTG TG-3'
mouse *Pfkl* qRT Re	5'-GTA GCC AGG TAGC CAC AG-3'
mouse *Tpi* qRT Fw	5'-TGC CAA ACA ATG AGC ACT GC-3'
mouse *Tpi* qRT Re	5'-ATC AGA AGC ATG TGA CCG GTG-3'
mouse *Aldoa* qRT Fw	5'-CTG GCC ATC ATG GAA AAT GC-3'
mouse *Aldoa* qRT Re	5'-TCA AGT CAT GGT CCC CAT CAG-3'
mouse *Aldob* qRT Fw	5'-ATC GGC GGA GTG ATC CTT TT-3'
mouse *Aldob* qRT Re	5'-TCC AAC TTG ATG CCC ACC A -3'
mouse *Gapdh* qRT Fw	5'-AGC CTC GTC CCG TAG ACA AAA-3'
mouse *Gapdh* qRT Re	5'-TGG CAA CAA TCT CCA CTT TGC-3'
mouse *Pgk1* qRT Fw	5'-TTT GGA CAA GCT GGA CGT GAA-3'
mouse *Pgk1* qRT Re	5'-GCT TGG AAC AGC AGC CTT GAT-3'
mouse *Pgam1* qRT Fw	5'-GTT GCG AGA TGC TGG CTA TGA-3'
mouse *Pgam1* qRT Re	5'-CAC ATC TGG TCA ATG GCA TCC-3'
mouse *Pgam2* qRT Fw	5’-TGG AAT GAG GAG ATC GCA CCT -3’
mouse *Pgam2* qRT Re	5’-TCG GAC ATC CCT TCC AGA TGT -3’
mouse *Eno1* qRT Fw	5'-TAT TGC GCC TGC TCT GGT TAG-3'
mouse *Eno1* qRT Re	5'-GGA TGG CAT TTG CAC CAA AT-3'
mouse *Eno3* qRT Fw	5'-GGA GAA GAA GGC CTG CAA TTG -3'
mouse *Eno3* qRT Re	5'-CCC AGC CAT TAG ATT GTG CAA -3
mouse *Pkm1* qRT Fw	5'-CTG TTT GAA GAG CTT GTG GCG -3
mouse *Pkm1* qRT Re	5'-CTG CTA AAC ACT TAT AAG AGG CC -3
mouse *p16INK4* qRT Fw	5'-CCC AAC GCC CCG AAC T -3'
mouse *p16INK4* qRT Re	5'-GCA GAA GAG CTG CTA CGT GAA -3

Table S3. Primers for real-time qRT-PCR (continued)

Name	Sequence
mouse *p21CIP1* qRT Fw	5'-AGA CAT TCA GAG CCA CAG GCA-3'
mouse *p21CIP1* qRT Re	5'- ATG AGC GCA TCGCAA TCA C -3
mouse *Bax* qRT Fw	5'-AGC AAA CTG GTG CTC AAG G -3'
mouse *Bax* qRT Re	5'-AGA CAA GCA GCC GCT CAC -3
mouse *Fas* qRT Fw	5'-CAG ACA TGC TGTGGA TCT GG -3'
mouse *Fas* qRT Re	5'-CCT CAG CTT TAA ACT CTC GGA -3
human *Rpl13a* qRT Fw	5'-CTG GAC CGT CTC AAG GTG TT -3'
human *Rpl13a* qRT Re	5'-GCC CCA GAT AGG CAA ACT T -3'
human *Hk1* qRT Fw	5'-ACA TTG TCT CCT GCA TCT CTG -3'
human *Hk1* qRT Re	5'-GCC TTA AAA CCC TTT GTC CAC -3'
human *Gpi* qRT Fw	5'-GCT TCT ACC AAT GGG CTC ATC -3'
human *Gpi* qRT Re	5'-TGT CCA GGA ACA TGC AGT G -3'
human *Pfkl* qRT Fw	5'-AAC GAG AAG TGC CAT GAC TAC -3'
human *Pfkl* qRT Re	5'-GTC CCA TAG TTC CGG TCA AAG -3'
human *Tpi* qRT Fw	5'-TCA TCG CAG ATA ACG TGA AGG -3'
human *Tpi* qRT Re	5'-CAT CAG AGA CGT TGG ACT TCA G -3'
human *Aldoa* qRT Fw	5'- GGT GTC ATC CTC TTC CAT GAG -3'
human *Aldoa* qRT Re	5'-GTA GTC TCG CCA TTT GTC CC -3'
human *Gapdh* qRT Fw	5'-CTT TGT CAA GCT CAT TTC CTG G -3'
human *Gapdh* qRT Re	5'-TCT TCC TCT TGT GCT CTT GC -3'
human *Pgk1* qRT Fw	5'- GCT TCT GGG AAC AAG GTT AAA G-3'
human *Pgk1* qRT Re	5'- CTG TGG CAG ATT GAC TCC TAC -3'
human *Pgam1* qRT Fw	5'-GGA GGC GCT CCT ATG ATG TC -3'
human *Pgam1* qRT Re	5'-ATC TTC TGT GAG GTC TGC ATA C -3'
human *Eno1* qRT Fw	5'- TTG GAG CAG AGG TTT ACC AC -3'
human *Eno1* qRT Re	5'- TTC CCA ATA GCA GTC TTC AGC-3'
human *Pkm1* qRT Fw	5'- CCA TAA TCG TCC TCA CCA AGT C-3'
human *Pkm1* qRT Re	5'- GGA AGA TGC CAC GGT ACA -3'
human *Chk1* qRT Fw	5'-GAG AAT CCA TCA GCA AGA ATT ACC -3'
human *Chk1* qRT Re	5'-GAA TGT GCT TAG AAA ATC CAC TGG-3'
human *Hif1* qRT Fw	5'-AAC ATA AAG TCT GCA ACA TGG AAG -3'
human *Hlf1* qRT Re	5'-TTT GAT GGG TGA GGA ATG GG -3'

Table S3. Primers for real-time qRT-PCR. Related to Figure 1 to 7
Sequences of primer used for real-time qRT-PCR in this study.

Transparent Methods

Cell culture

The human cell lines H1299, RKO, SW480, DLD-1, HT-29, Hs578t, MDA-MB-231, BT-474, U2OS, and SJSA-1 were obtained from American Type Culture Collection, and HCT116, Hek293, HepG2, and WI-38 were from RIKEN Bioresources Center. HSC-1 and HSC-5 were obtained from the Japanese Collection of Research Bioresources. The PLAT-A packaging cell line was a kind gift from Dr. Toshio Kitamura (University of Tokyo). The human cell lines (H1299, Hs578t, MDA-MB-231, BT-474, HCT116, RKO, SW480, DLD-1, HT-29, HEK293, HepG2, SJSA-1, U2OS, and WI-38) were cultured in Dulbecco's modified Eagle medium (DMEM) containing 10% fetal bovine serum (FBS). HSC-1 cells were cultured in DMEM with 20% FBS. HSC-5 cells were cultured in Iscove's modified Dulbecco's medium with 10% FBS. MEFs isolated from embryos (postcoital day 13.5) of C57BL/6 mice were grown in DMEM with 10% FBS and antibiotics (Carnero et al., 2000). *Pgam1*$^{flox/flox}$ *ER-Cre* MEFs were generated by crossing between *CAG-ER-Cre* mice (Hayashi and McMahon, 2002) and *Pgam1*$^{flox/flox}$ mice. At passage 4, *Pgam1*$^{flox/flox}$ *ER-Cre* MEFs or *Pgam1*$^{flox/fox}$ MEFs were treated with 0.5 μM 4-OHT for 4 days. Ablation of PGAM was detected by immunoblotting. All cell lines were tested and shown to be negative for mycoplasma contamination.

Cytochemical staining for SA-β-Gal was performed (Dimri et al., 1995). At passage 6 and 10, *Pgam1*$^{flox/flox}$ *ER-Cre* or *Pgam1*$^{flox/flox}$ MEFs were washed twice with ice-cold phosphate-buffered saline (PBS) buffer and were treated by fixation solution (2% formaldehyde and 0.2 % glutaraldehyde in PBS buffer) for 5 min at room temperature. After removing the fixation solution, cells were washed twice with PBS buffer and were incubated with staining solution (40 mM citric acid /Na phosphate buffer, 5 mM $K_4[Fe(CN)6]$ $3H_2O$, 5 mM $K_3[Fe(CN)_6]$, 150 mM NaCl, 2 mM $MgCl_2$, 1 mg/ml X-gal) for overnight at 37°C. Images were recorded using a microscope (IX-73, Olympus, Tokyo, Japan),

Cells were subjected to retroviral infection or transfection of plasmids. For the proliferation assay, 5×10^3 cells were plated on 6-cm dishes. After 10 days of culture, cells were fixed with 2% glutaraldehyde, followed by crystal violet staining. Then the staining was resolved by 1% sodium dodecyl sulfate. The optical density was determined at 590 nm.

Plasmid DNA

Expression of full-length mouse *Pgam1* and *Pgam2* with a C-terminal 3X FLAG tag and deletion mutants of *Pgam2* (TN, T4, and TC) with a C-terminal 3X FLAG tag driven by the CMV promoter of the p3xFLAG-CMV14 expression vector were constructed previously (Mikawa et al., 2014). The deletion mutants of *Pgam1* (TN, T4, and TC) with a C-terminal 3X FLAG tag were generated by PCR. The relevant variants of *Pgam1* and *Pgam2* mutamts *(W68A*, *W78A and R90W*) were generated

by PCR-based mutagenesis. pHygro MarxIV retroviral vectors encoding mouse *Pgam1* and *Pgam2* variants were also generated. The relevant variant *Pgam1* and *Pgam2* cDNAs were ligated into the XhoI site of Hygro Marx IV vectors. The pBabe-puro-Ras-G12V plasmid was a gift from Dr. Kayoko Maehara (Kio University, Nara, Japan). The pcDNA3.1 Chk1-myc-his vector was previously described (Niida et al., 2007). *Chk1* cDNAs were sub-cloned into WZLneo retroviral vectors. Human *p53* cDNA was sub-cloned into the pcDNA3.1 vector containing a 3X HA sequence between the NheI and XhoI sites. Expression of full-length p53 with an N-terminal 3X HA-tag was driven by the CMV promoter. Expression vector of human Mdm2 with an N-terminal HA-tag was constructed previously (Mikawa et al., 2014). NanoBiT vectors were generated using Flexi Vector Systems (Promega). In brief, wild type and relevant mutants of *Pgam1* and *Pgam2 (W68A*, *W78A*) were subcloned into pF4A plasmid. Subsequently, those relevant variants of Pgam were subcloned into N-terminus LgBiT-tagging plasmid (pFN33K) or SmBiT-tagging plasmid (pFN35K).

Reagents

Reagents were obtained as follows. UCN01, DMBA, TPA, and Nutlin-3a from Sigma–Aldrich (St. Louis, MO). MG132 from Peptide Institute, Inc. (Osaka, Japan). U126 and Triciribine from FUJIFILM Wako Pure Chemical Corporation (Osaka, Japan). BI D-1870 from Selleck (Houston, TX).

Mouse models

All procedures for animal experiments were performed in accordance with the principles and guidelines of the Animal Care and Use Committees of Kyoto University Graduate School of Medicine.

Pgam2-Tg mice were generated previously (Mikawa et al., 2014). *Pgam2-Tg* is a strain of transgenic C57BL/6 mice that overexpresses the *Pgam2* with a 3xFLAG tag under the cytomegalovirus immediate-to-early enhancer element and chicken *β-actin* promoter (*CAG*) (Niwa et al., 1991) For generation of the *Pgam1* KO mouse, the targeting vector was constructed as follows. Exons 2–4 of mouse *Pgam1* were flanked by two loxP sequences, and a FLP recognition target (*FRT*)-flanked neo-cassette was inserted upstream of exon 2. The targeting vector was introduced into mouse embryonic stem cells (C57BL/6), which were injected into blastocysts (BALB/c). Generated founder mice ($Pgam1^{flox/+}$ [neo+]) were crossed with *FLP* transgenic mice for removal of the neo-cassette from heterozygous *flox* mice. $Pgam1^{+/-}$ mice were generated by crossing $Pgam1^{flox/+}$ mice and *CAG-Cre* Tg mice, which ubiquitously express Cre recombinase under the *CAG* promoter. Genotyping was performed using PCR.

Mouse experiments

For assessment of inflammatory response, control or *Pgam2-Tg* mice (18 weeks old, male) were treated with 10 ng TPA on the ears, and the thickness of the ears was measured by constant pressure thickness gauge (PG-201, TECLOCK, Japan).

Chemically induced skin tumorigenesis was performed (Takeuchi et al., 2010). Briefly, seven age-matched (12–15 weeks old, male) pairs of control or *Pgam2-Tg* mice were shaved and treated with 100 μg DMBA in 100 μl acetone. Mice were subsequently treated twice weekly with 12.5 μg TPA in 100 μl acetone for 20 weeks. The number and size of papillomas per mouse were recorded every 2 weeks. The nude mouse xenograft assay was performed (Mikawa et al., 2014). *CAnN.Cg-Foxn^{nu}/CrlCrlj* mice (8 weeks old, male) were injected subcutaneously with 5 × 10^6 cells suspended in 100 μl phosphate-buffered saline. Tumor formation was assessed after 2 weeks.

Transfection and retroviral infection

Transfection of siRNA for mouse *Pgam1*, human *Pgam1* (Life Technologies, Carlsbad, CA), and human *Chk1* (Sigma–Aldrich, St. Louis, MO) was performed using Lipofectamine siRNA MAX (Invitrogen, Carlsbad, CA). Expression vectors were transfected by polyethylenimine MAX (Polysciences, Warrington, PA). The PLAT-A packaging cell line was used for retroviral production (Morita et al., 2000). Retrovirus-infected cells were treated with hygromycin (75 μg/mL), G418 (400 μg/mL), or puromycin (2 μg/mL) for positive selection of infected cells.

Immunoblotting and immunoprecipitation

For immunoblotting, cell lysates were prepared (Carnero *et al.*, 2000). Cells were washed twice with ice-cold PBS and lysed in buffer containing 50 mM Tris–HCl (pH 7.5), 200 mM NaCl, 1 mM ethylenediaminetetraacetic acid (EDTA), 10% glycerol, 0.5% Triton-X100, 50 mM NaF, 1 mM dithiothreitol (DTT), 1 mM Na_3VO_4, 1 mM phenylmethanesulfonyl fluoride (PMSF), and protease inhibitor cocktail (Sigma–Aldrich). After 30 min on ice, lysates were cleared by centrifugation. Equivalent amounts of protein were resolved by sodium dodecyl sulfate-polyacrylamide gel electrophoresis (SDS-PAGE). Anti-PGAM antibody (1:1000), which recognizes both PGAM1 and PGAM2 (Mikawa *et al.*, 2014). Anti-FLAG (F1804, 1:1000), anti-human Chk1 (C9358, 1:3000), and anti-Actin (A4700, 1:1000) from Sigma–Aldrich. Anti-$p21^{CIP1}$ (ab7960, 1:500), anti-phospho-p53 (Ser23; ab59206, 1:500), anti-Chk2 (ab8108, 1:1000), anti-Aldolase (ab169544, 1:1000), anti-PGK1 (ab38007, 1:1000), anti-ENO1 (ab155102, 1: 1000), anti-PGAM1 (ab129191, 1:1000) and anti-PGAM2 (ab183027, 1:1000) from Abcam (Cambridge, UK). Anti-c-myc (9E10, 1: 200), anti-

human p53 (DO-1, 1:1000), anti-mouse Chk1 (Sc-8404, 1:1000) and anti-Mdm2 (SMP-14, 1:200) from Santa Cruz Biotechnology (Dallas, TX). Anti-mouse p53 (1C12; #2524, 1:1000), anti-phospho-p53 (Ser20; #9287, 1:200), anti-phospho-p53 (Ser15; #9284, 1:1000), anti-phospho-Chk1 (Ser345; #2341, 1:1000), and anti-phospho-Chk2 (Thr68; #2661, 1:500), anti-ERK1/2 (#4370, 1:2000), anti-phospho-ERK1/2 (Thr202/Tyr204, #4370, 1:2000), anti-Bad (#9339, 1:1000), anti-phospho-Bad (Ser112, #9391, 1:500), anti-Akt(pan) (#4691, 1:1000) and anti-phospho-Akt (Ser473, #9271, 1:1000) from Cell Signaling Technology (Danvers, MA). Anti-GAPDH (MAB374, 1:3000) from Merck Milipore (Burlington, MA).

For immunoprecipitation assays, cell lysates were precipitated with the relevant antibody for 2 h. Immune complexes were recovered with protein G-agarose beads, washed four times with lysis buffer, and boiled in 2× Laemmli sample buffer for 5 min. Denatured immune complexes were resolved by SDS-PAGE. The quantification of the immunoblot bands were performed using ImageJ.

Dimer and monomer forms of proteins were detected by the modification of the previous protocol as follows (Jagemann et al., 2008). Cultured cells were lysed with lysis buffer (50 mM Tris–HCl (pH 7.5), 150 mM NaCl, 1 mM EDTA, 10% glycerol, 0.5% Triton-X100, 50 mM NaF, 1 mM Na_3VO_4, 1 mM PMSF and protease inhibitor cocktail (Sigma–Aldrich). After the fractionation by centrifugal 100 kDa cutoff filter (Amicon Ultra-4, Merck Milipore Ltd) for 45 min, the resulting extracts were immunoprecipitated by anti-PGAM1 antibody (ab2220, Abcam) for 2 hours. Immunoprecipitants were incubated with 100 μg/ml synthetic peptide (KAMEAVAAQGKAKK), whose sequence matched with those in C-terminus of PGAM1 protein, the antigenic determinant of anti-PGAM1 antibody. Eluted PGAM proteins were cross-linked by 0.5% glutaraldehyde for 5 min at 37°C. Forms of PGAM proteins were evaluated by immunoblotting.

Measurement of glycolytic enzyme activity

Enzymatic activity of aldolase, GAPDH, PGK and enolase were measured spectrophotometrically using enzyme activity assay kit (BioVision, Milpitas, CA). PGAM enzymatic activity was measured (Kondoh et al., 2005). Briefly, cell lysates or recombinant proteins were incubated in reaction buffer (100 mM Tris–HCl [pH 8.0], 100 mM KCl, 0.5 mM EDTA, 2 mM $MgCl_2$, 0.2 mM NADH, 3 mM ADP, and 10 μM 2,3-diphosphoglycerate) with enzyme mixture (0.6 U lactate dehydrogenase, 0.5 U pyruvate kinase, and 0.1 U enolase). Next, 1mM 3-phosphoglyceric acid was added and incubated at 37°C. Activity was measured as NAD^+ release.

Glycolytic flux measurement

Glycolytic flux was measured (Kondoh et al., 2005). After cells were cultured for 11 h in DMEM containing 25 mM glucose, medium was exchanged for DMEM containing 4.25 mM glucose. After 10 h, D-[3-^{3}H] glucose was added to the medium. After 6 h, an aliquot of medium was precipitated with perchloric acid. The supernatant was applied to a column filled with DOWEX 1X8 200–400 MESH Cl resin (Sigma–Aldrich), and the amount of [^{3}H] water in the flow through was normalized to protein content. The glucose and lactate concentrations in the culture medium were determined using a glucose or lactate assay kit (BioVision), respectively. The value of glucose consumption or lactate production was normalized to the protein content of the corresponding cell lysate.

RNA analysis

Total RNA was extracted with TRIzol (Invitrogen). cDNA pools were generated using the ReverTra Ace qPCR RT kit (Toyobo, Osaka, Japan). Real-time quantitative PCR was performed using the Thermal Cycler Dice Real-Time system (Takara Bio., Kusatsu, Japan) and Thunderbird SYBR qPCR mix (Toyobo). Gene expression levels were normalized to *Rpl13a* mRNA and presented as values relative to controls. The primers used are shown in Table S3.

***In vitro* phosphatase assay**

Phosphatase activity was determined using a serine/threonine phosphatase assay system (Promega). Phosphopeptides were obtained from Scrum Inc. (Tokyo, Japan). Briefly, 5000 pmol phosphopeptide was preincubated in various pH conditions (pH 6.2, 7.2, 8.2, and 9.2) in phosphatase reaction buffer (50 mM imidazole, 0.2 mM ethylene glycol-bis(β-aminoethyl ether)-N,N,N',N'-tetraacetic acid, 5 mM $MgCl_2$, 0.02% beta-mercaptoethanol, and 0.1 mg/mL bovine serum albumin) for 3 min at 30°C (Dhananjaya and D'Souza, 2011). Recombinant PGAM protein or λPPase was added to the reaction and incubated for 30 min at 30°C. Free phosphate was detected as the absorbance by the complex of molybdate, malachite green, and phosphate, according to the manufacturer's protocol. RRA(pT)VA phosphopeptide is compatible as a substrate for several serine/threonine phosphatases such as protein phosphatases 2A, 2B, and 2C (Donella Deana et al., 1990). For assessment of phosphatase activity against phospho-p53 (Ser15), phospho-p53 (Ser20), and phospho-p53 (Ser15 and Ser20) peptides, 5000 pmol phosphopeptides were incubated with 500 ng recombinant PGAM1 or PGAM2 protein or 250 ng λPPase in phosphatase reaction buffer (pH 7.2). The phospho-p53 peptide sequences were described previously (Shreeram

et al., 2006).

NanoBiT assay

NanoLuc Binary Technology (NanoBiT) assay (Promega) is utilized to quantify protein-protein interaction between the proteins with large and small NanoBiT tag (Dixon et al., 2016). NanoLuc is newly invented smaller luciferase than standard luciferase, but much more stable with production of much brighter luminescence. NanoBiT comprises two complementary small and large subunits (SmBiT and LgBiT, respectively), whose assembly generates luminescence. This technology was applied for accurate measurement of protein interactions (Song et al., 2020). We generated recombinant PGAM1, 2-WT, W68A, and W78A proteins with NanoBiT tags from the extract of bacteria. A saturation assay was performed using low levels (0.25 nM) of SmBiT fusion proteins for the binding with LgBiT partners at increasing concentrations (0.98 to 500 nM). LgBiT fusion proteins were incubated with or without SmBiT fusion protein in binding buffer (1% BSA in PBS) for 60 min. At the end of incubation, binding intensity was measured as luminescent emission by GloMAX navigator (Promega). Specific binding intensity was obtained by subtraction of background signal (luminescence of LgBiT protein only) from total binding signal (luminescence of LgBiT protein with SmBit protein). For estimation of binding dissociation constant (Kd), we used 1:1 binding model and the curve of specific binding was fitted using GraphPad prism 8 (GraphPad software, CA).

Prognosis analysis

The correlation between the expression level of PGAM1 or Chk1 and the survival rates of NSCLC patients was assessed by the minimum P-value approach using the PrognoScan database (Mizuno et al., 2009). Dataset of Jacob-00182-MSK was evaluated (Director's Challenge Consortium for the Molecular Classification of Lung et al., 2008). NSCLC patients were classified into two groups according to PGAM1 or Chk1 expression levels in their tumors at all possible cutoff points. The P-value of risk differences between any two groups were analyzed using the log-rank test. The cutoff was selected at the point giving the most significant P-value.

Statistical analysis

All data are expressed as the mean ± standard error of the mean (SEM) from at least three independent experiments. Comparisons between two independent groups were analyzed using an unpaired Student's two-tailed t-test. Comparisons between multiple groups were analyzed using one-way analysis of variance and Dunnett's multiple comparison test.

Supplemental references

Barretina, J., Caponigro, G., Stransky, N., Venkatesan, K., Margolin, A.A., Kim, S., Wilson, C.J., Lehar, J., Kryukov, G.V., Sonkin, D.*, et al.* (2012). The Cancer Cell Line Encyclopedia enables predictive modelling of anticancer drug sensitivity. Nature *483*, 603-607.

Carnero, A., Hudson, J.D., Price, C.M., and Beach, D.H. (2000). p16INK4A and p19ARF act in overlapping pathways in cellular immortalization. Nature cell biology *2*, 148-155.

Chen, J.Y., Funk, W.D., Wright, W.E., Shay, J.W., and Minna, J.D. (1993). Heterogeneity of transcriptional activity of mutant p53 proteins and p53 DNA target sequences. Oncogene *8*, 2159-2166.

Dhananjaya, B.L., and D'Souza, C.J. (2011). The pharmacological role of phosphatases (acid and alkaline phosphomonoesterases) in snake venoms related to release of purines - a multitoxin. Basic Clin Pharmacol Toxicol *108*, 79-83.

Dimri, G.P., Lee, X., Basile, G., Acosta, M., Scott, G., Roskelley, C., Medrano, E.E., Linskens, M., Rubelj, I., Pereira-Smith, O.*, et al.* (1995). A biomarker that identifies senescent human cells in culture and in aging skin in vivo. Proceedings of the National Academy of Sciences of the United States of America *92*, 9363-9367.

Donella Deana, A., Mac Gowan, C.H., Cohen, P., Marchiori, F., Meyer, H.E., and Pinna, L.A. (1990). An investigation of the substrate specificity of protein phosphatase 2C using synthetic peptide substrates; comparison with protein phosphatase 2A. Biochim Biophys Acta *1051*, 199-202.

Fujita, T., Kiyama, M., Tomizawa, Y., Kohno, T., and Yokota, J. (1999). Comprehensive analysis of p53 gene mutation characteristics in lung carcinoma with special reference to histological subtypes. Int J Oncol *15*, 927-934.

Hayashi, S., and McMahon, A.P. (2002). Efficient recombination in diverse tissues by a tamoxifen-inducible form of Cre: a tool for temporally regulated gene activation/inactivation in the mouse. Dev Biol *244*, 305-318.

Iwakawa, R., Kohno, T., Enari, M., Kiyono, T., and Yokota, J. (2010). Prevalence of human papillomavirus 16/18/33 infection and p53 mutation in lung adenocarcinoma. Cancer Sci *101*, 1891-1896.

Jagemann, L.R., Perez-Rivas, L.G., Ruiz, E.J., Ranea, J.A., Sanchez-Jimenez, F., Nebreda, A.R., Alba, E., and Lozano, J. (2008). The functional interaction of 14-3-3 proteins with the ERK1/2 scaffold KSR1 occurs in an isoform-specific manner. J Biol Chem *283*, 17450-17462.

Kashii, T., Mizushima, Y., Monno, S., Nakagawa, K., and Kobayashi, M. (1994). Gene analysis of K-, H-ras, p53, and retinoblastoma susceptibility genes in human lung cancer cell lines by the polymerase chain reaction/single-strand conformation polymorphism method. J Cancer Res Clin Oncol *120*, 143-148.

Kaufman, J.M., Yamada, T., Park, K., Timmers, C.D., Amann, J.M., and Carbone, D.P. (2017). A Transcriptional Signature Identifies LKB1 Functional Status as a Novel Determinant of MEK Sensitivity in Lung Adenocarcinoma. Cancer research *77*, 153-163.

Morita, S., Kojima, T., and Kitamura, T. (2000). Plat-E: an efficient and stable system for transient packaging of retroviruses. Gene Ther *7*, 1063-1066.

Nagai, Y., Miyazawa, H., Huqun, Tanaka, T., Udagawa, K., Kato, M., Fukuyama, S., Yokote, A., Kobayashi, K., Kanazawa, M*., et al.* (2005). Genetic heterogeneity of the epidermal growth factor receptor in non-small cell lung cancer cell lines revealed by a rapid and sensitive detection system, the peptide nucleic acid-locked nucleic acid PCR clamp. Cancer research *65*, 7276-7282.

Niida, H., Katsuno, Y., Banerjee, B., Hande, M.P., and Nakanishi, M. (2007). Specific role of Chk1 phosphorylations in cell survival and checkpoint activation. Mol Cell Biol *27*, 2572-2581.

Niwa, H., Yamamura, K., and Miyazaki, J. (1991). Efficient selection for high-expression transfectants with a novel eukaryotic vector. Gene *108*, 193-199.

Shreeram, S., Demidov, O.N., Hee, W.K., Yamaguchi, H., Onishi, N., Kek, C., Timofeev, O.N., Dudgeon, C., Fornace, A.J., Anderson, C.W*., et al.* (2006). Wip1 phosphatase modulates ATM-dependent signaling pathways. Molecular cell *23*, 757-764.

Notsuda, H., Sakurada, A., Endo, C., Okada, Y., Horii, A., Shima, H., and Kondo, T. (2013). p190A RhoGAP is involved in EGFR pathways and promotes proliferation, invasion and migration in lung adenocarcinoma cells. Int J Oncol *43*, 1569-1577.

Shreeram, S., Demidov, O.N., Hee, W.K., Yamaguchi, H., Onishi, N., Kek, C., Timofeev, O.N., Dudgeon, C., Fornace, A.J., Anderson, C.W*., et al.* (2006). Wip1 phosphatase modulates ATM-dependent signaling pathways. Molecular cell *23*, 757-764.

Song, X., Yu, Y., Shen, C., Wang, Y., and Wang, N. (2020). Dimerization/oligomerization of the extracellular domain of the GLP-1 receptor and the negative cooperativity in its ligand binding revealed by the improved NanoBiT. FASEB J *34*, 4348-4368.

Takeuchi, S., Takahashi, A., Motoi, N., Yoshimoto, S., Tajima, T., Yamakoshi, K., Hirao, A., Yanagi, S., Fukami, K., Ishikawa, Y*., et al.* (2010). Intrinsic cooperation between p16INK4a and p21Waf1/Cip1 in the onset of cellular senescence and tumor suppression in vivo. Cancer research *70*, 9381-9390.

Wei, S., Liu, T., Liu, H., and Gao, J. (2003). Unique GGT --> GTT mutation at K-ras codon 12 in six human pancreatic cancer cell lines from Chinese patients. Chin Med J (Engl) *116*, 1585-1587.